1   **AKAP79 enables calcineurin to directly suppress protein kinase A activity**

2

3   Timothy W. Church[a], Parul Tewatia[b,c], Saad Hannan[a], João Antunes[b], Olivia Eriksson[b], Trevor G. Smart[a],

4   Jeanette Hellgren Kotaleski[b,c], Matthew G. Gold[a,1]

5

6

7   [a]Department of Neuroscience, Physiology & Pharmacology, University College London, Gower Street,

8   LONDON, WC1E 6BT, UK

9

10   [b]Science for Life Laboratory, School of Computer Science and Communication, KTH Royal Institute of

11   Technology, Stockholm, Sweden

12

13   [c]Department of Neuroscience, Karolinska Institute, Solna, Sweden

14

15   [1]Correspondence: m.gold@ucl.ac.uk

16

17

18

19   **Abstract**

20

21   Interplay between the second messengers cAMP and Ca^{2+} is a hallmark of dynamic cellular processes. A

22   common motif is the opposition of the Ca^{2+}-sensitive phosphatase calcineurin and the major cAMP receptor,

23   protein kinase A (PKA). Calcineurin dephosphorylates sites primed by PKA to bring about changes

24   including synaptic long-term depression (LTD). AKAP79 supports signaling of this type by anchoring PKA

25   and calcineurin in tandem. In this study, we discovered that AKAP79 increases the rate of calcineurin

26   dephosphorylation of type II PKA regulatory subunits by an order of magnitude. Fluorescent PKA activity

27   reporter assays, supported by kinetic modeling, show how AKAP79-enhanced calcineurin activity enables

28   suppression of PKA without altering cAMP levels by increasing PKA catalytic subunit capture rate.

29   Experiments with hippocampal neurons indicate that this mechanism contributes towards LTD. This non-

30   canonical mode of PKA regulation may underlie many other cellular processes.

31

32

33

Introduction

Cyclic adenosine monophosphate (cAMP) and Ca^{2+} are ancient second messengers that are fundamental to the regulation of many dynamic cellular processes including synaptic plasticity (Huang et al., 1994), heart contraction (Bers et al., 2019), and glycogen metabolism (Roach et al., 2012). Crosstalk between the two second messengers is a common feature of cellular signaling. For example, cAMP can enhance cytosolic Ca^{2+} entry by triggering phosphorylation of key ion channels (Qian et al., 2017; Schmitt et al., 2003) by its major intracellular receptor cAMP-dependent protein kinase, also known as Protein Kinase A (PKA). Similarly, Ca^{2+} can regulate cAMP levels by altering activities of both phosphodiesterases (Baillie et al., 2019) and adenylyl cyclases (Qi et al., 2019). At the receptor level, a common signaling motif is the opposition of PKA and the highly-abundant Ca^{2+}-sensitive phosphatase calcineurin (CN), with CN triggering cellular changes by removing phosphate from substrates primed by PKA. Notable examples of this motif are the regulation of postsynaptic substrates including AMPA-type glutamate receptors in the induction of long-term depression (LTD) of synaptic strength (Bear, 2003), and control of NFAT nuclear localization in immune responses (Hogan, 2017). According to current consensus, in these cases CN dephosphorylates substrates without any requirement for directly altering PKA activity (Dittmer et al., 2014; Lu et al., 2011; Tunquist et al., 2008; Weisenhaus et al., 2010; Zhang & Shapiro, 2016). This implies that energetically-costly futile cycles of phosphate addition and removal by PKA and CN must persist to maintain dephosphorylated substrate. It would be more logical for PKA activity to be switched off when CN is activated during substrate dephosphorylation. Uncovering the mechanism to achieve this is the focus of this study.

Recent years have seen renewed interest in mechanisms for regulating the release and re-capture of PKA catalytic subunits (Bock et al., 2020; Gold, 2019; Zhang et al., 2020), including new data that hint at how CN might directly suppress PKA activity. PKA is comprised of regulatory subunit dimers that bind and sequester PKA catalytic (C) subunits in an inhibited state (Taylor et al., 2019). PKA regulatory subunits are classified into type I subunits (RIα and RIβ) that are predominantly cytosolic, and type II subunits (RIIα and RIIβ) that co-sediment with membranes (Gold, 2019). The regulatory subunit inhibitor sequence (IS) is phosphorylated upon association with C subunits for RII but not RI subunits, which bear alanine in place of serine in the phospho-acceptor site (S98 in RIIα). Quantitative immunoblotting and mass spectrometry (MS) have recently shown that PKA regulatory subunits – and particularly RII subunits – greatly outnumber PKA C subunits (Aye et al., 2010; Walker-Gray et al., 2017) throughout the body. In addition, Zhang and co-workers (Zhang et al., 2015) have extended earlier observations (Rangel-Aldao & Rosen, 1976) to quantify differences in the rate of C subunit binding to RII subunits either phosphorylated (pRII) or

68 dephosphorylated at the IS. Remarkably, the k_{on} rate for C subunit association is ~50 times faster for

69 dephosphorylated RII than pRII (Zhang et al., 2015) (*Figure 1*A). In theory, rapid dephosphorylation of

70 RII subunits by CN could directly suppress PKA activity by increasing the rate of C subunit capture thereby

71 reducing the proportion of C subunits that are dissociated (Buxbaum & Dudai, 1989; Isensee et al., 2018).

72 While recent observations concerning PKA subunit stoichiometry and pRII/RII binding kinetics support

73 this notion, isolated pRII is a low affinity substrate for CN with a half-maximal substrate concentration

74 (K_m) above 20 µM (Perrino et al., 1992; Stemmer & Klee, 1994). Therefore, pRII dephosphorylation by

75 CN would not be expected to occur to a meaningful degree at physiological concentrations in the absence

76 of an additional factor.

77

78 Anchoring proteins support signal transduction by elevating effective local concentrations of signaling

79 proteins. A-kinase anchoring protein 79 (AKAP79; rodent ortholog AKAP150, gene name AKAP5) is a

80 prototypical mammalian anchoring protein with several features that indicate it could operate in part by

81 increasing the effective protein concentration of pRII subunits for CN. AKAP79 can simultaneously anchor

82 both CN and PKA (Coghlan et al., 1995). It contains an amphipathic anchoring helix (Gold et al., 2006;

83 Kinderman et al., 2006) for binding RII subunits, and a short linear 'PIAIIIT' CN anchoring motif

84 (Dell'Acqua et al., 2002; Li et al., 2012). The two anchoring sites are separated by only ~50 amino acids in

85 the primary sequence within the C-terminus of AKAP79 (*Figure 1*B). AKAP79 is localized in dendritic

86 spines where it is required for anchoring RII subunits (Tunquist et al., 2008). The anchoring protein is

87 necessary for both induction of long-term depression (LTD) of CA3-CA1 hippocampal synapses (Lu et al.,

88 2008; Tunquist et al., 2008; Weisenhaus et al., 2010), and for CN-mediated dephosphorylation of NFAT

89 (Kar et al., 2014; Murphy et al., 2014) – both processes that are driven by CN dephosphorylation of sites

90 primed by PKA. Despite these characteristics, the possibility that AKAP79 could support pRII

91 dephosphorylation by CN has been disregarded perhaps because paradoxically AKAP79 acts as a weak

92 inhibitor for CN dephosphorylation of 20-mer peptides corresponding to the phosphorylated RII IS

93 (Coghlan et al., 1995; Kashishian et al., 1998). We reasoned that these assays could be misleading since

94 peptide substrates are not subject to anchoring alongside CN that occurs for full-length RII subunits. To

95 resolve this issue, in this study we measured how AKAP79 alters CN activity towards full-length pRII

96 subunits. We went on to determine if AKAP79 can reduce the fraction of dissociated C subunits in concert

97 with CN using fluorescence-based assays supported by kinetic modeling, before substantiating our

98 observations in hippocampal neurons.

99

100

101 **Results**

102

103 **AKAP79 enables CN to efficiently dephosphorylate RII subunits at physiological concentrations**

104 We set out to determine whether AKAP79 can increase CN dephosphorylation of full-length RII subunits

105 phosphorylated at the IS. Using purified proteins (*Figure 1-figure supplement 1*), we compared ^{32}P release

106 from either pRIIα (*Figure 1*C) or pRIIβ (*Figure 1*D). Thirty second reactions were initiated by addition of

107 excess Ca^{2+}/calmodulin (CaM) to 10 nM CN and 400 nM pRII subunits. For pRIIα without AKAP79,

108 phosphate was released from only 0.36±0.13 % of the subunits (black, *Figure 1*C). Inclusion of full-length

109 AKAP79 in the reaction mix increased phosphate release by 12.4-fold ($p = 7.4 \times 10^{-6}$) to 4.52±0.26 % pRIIα

110 subunits (light blue, *Figure 1*C). Removing the PIAIIIT anchoring sequence in AKAP79 (ΔCN) returned

111 dephosphorylation to a baseline level of 0.26±0.06 % (grey, *Figure 1*C), consistent with a mechanism in

112 which anchoring of CN adjacent to pRII subunits enhances the rate of dephosphorylation. Similar results

113 were obtained for pRIIβ, with addition of AKAP79 increasing phosphate release 16.3-fold ($p = 3.0 \times 10^{-6}$)

114 from 0.34±0.13 % (black, *Figure 1*D) to 5.49±0.17 % (dark blue, *Figure 1*D). Ablating the CN anchoring

115 site in AKAP79 also reduced phosphorylation to a baseline level of 0.2±0.02 % for this isoform (grey,

116 *Figure 1*D).

117

118 We next measured CN phosphatase towards pRII over a range of pRII concentrations. We compared

119 activity towards pRII subunits alone or in complex with a fragment of AKAP79 (AKAP79$_{c97}$) encompassing

120 positions 331-427 that includes the CN and RII subunit anchoring sites. Working with this stable highly-

121 expressed construct enabled us to purify sufficient quantities of pRIIα-AKAP79$_{c97}$ and pRIIβ-AKAP79$_{c97}$

122 complexes (*Figure 1-figure supplement 1*C & D) to sample concentrations up to 5 μM. In complex with

123 AKAP79$_{c97}$, both pRIIα and pRIIβ acted as relatively high affinity substrates of CN. pRIIα-AKAP79$_{c97}$

124 (light blue, *Figure 1*E) was dephosphorylated with a half-maximal concentration (K$_m$) of 1.36±0.16 μM

125 and turnover number (k$_{cat}$) of 0.45±0.02 s^{-1}, and pRIIβ-AKAP79$_{c97}$ with K$_m$ = 0.74±0.12 μM and k$_{cat}$ =

126 0.24±0.01 s^{-1}. As expected, in the absence of the anchoring protein, pRIIα and pRIIβ subunits served as low

127 affinity substrates for CN (black lines, *Figure 1*E & F). For both isolated pRII isoforms, the relationship

128 between phosphatase activity and pRII concentration was linear up to 20 μM (*Figure 1-figure supplement*

129 *2*) – the highest concentration tested – indicative of a K$_m$ of greater than 20 μM. CN activity was very low

130 (<0.03 s^{-1}) at concentrations of 5 μM pRII or lower. This is consistent with earlier studies that reported a

131 K$_m$ of 94 μM for CN dephosphorylation of a phosphorylated 19-mer peptide derived from the RIIα IS

132 (Stemmer & Klee, 1994).

133
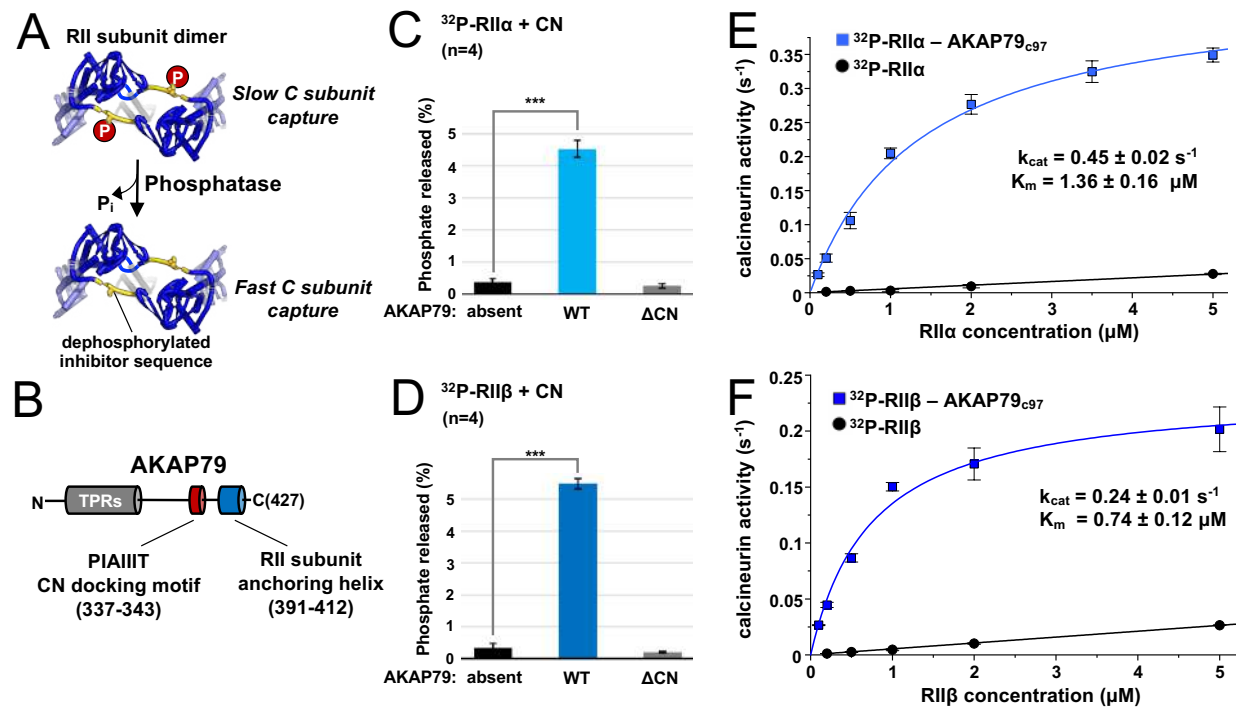
Figure 1. Effect of AKAP79 on pRII dephosphorylation by CN. (**A**) Dephosphorylation of the inhibitor sequence (IS, yellow) of RII subunits enables faster PKA C subunit capture. (**B**) AKAP79 contains anchoring sites for CN (red) and PKA RII subunits (blue) in its C-terminal region. Other macromolecular interactions are mediated through elements within its tandem polybasic regions (TPRs, grey). (**C**) CN-catalyzed phosphate release from pRIIα subunits with either no AKAP79, WT AKAP79 (light blue), or AKAP79 lacking the PIAIIIT anchoring motif ('ΔCN'). (**D**) CN-catalyzed phosphate release from pRIIβ subunits with either no AKAP79, WT AKAP79 (dark blue), or AKAP79 ΔCN. (**E**) The relationship between CN activity towards pRIIα subunits and pRIIα concentration with pRIIα subunits included either alone (black circles) or in complex with AKAP79$_{c97}$ (light blue squares). (**F**) The relationship between CN activity towards pRIIβ subunits and pRIIβ concentration with pRIIβ subunits included either alone (black circles) or in complex with AKAP79$_{c97}$ (dark blue squares). For panels E & F, activities at each concentration were measured in triplicate. Statistical comparisons were performed using two-tailed unpaired Student t-tests. ***$p<0.001$.

To put our kinetic parameters for pRII dephosphorylation into a physiological context, we set out to determine accurate protein concentrations for PKA subunits in the CA1 neuropil where Schaffer collaterals from the CA3 region synapse onto CA1 dendrites (*Figure 2*A). These synapses are a leading prototype for understanding forms of LTD driven by CN following PKA priming (Bear, 2003). We collected hippocampal slices from 18-day old male Sprague-Dawley rats before micro-dissecting CA1 neuropil sections (*Figure 2*B). Following homogenization, concentrations of C, RIIα, RIIβ, and RI subunits in the extracted protein were determined using quantitative immunoblotting by running extracts (n=5) alongside

reference concentrations of purified PKA subunits (*Figure 2*C, *Figure 2-figure supplement 1*) (Walker-Gray et al., 2017). We found that RIIα was by far the most predominant PKA subunit in the CA1 neuropil, accounting for 0.32±0.029 % total protein content compared to 0.032±0.003 % for C subunits, 0.041±0.014 % for RI, and 0.06±0.006 % for RIIβ. These numbers equate to a 9.4-fold higher molar abundance of RIIα subunits (light blue, *Figure 2*D) relative to C subunits with RI and RIIβ present at similar levels to C subunits. The predominance of the RIIα subunit is consistent with a previous imaging study of rodent hippocampus (Weisenhaus et al., 2010). Assuming that protein accounts for 8 % of total rat brain weight (Clouet & Gaitonde, 1956), we estimated RII subunit concentrations of 5.9 µM (RIIα) and 1.03 µM (RIIβ). These values fall within the range where CN efficiently dephosphorylates pRII only in the presence of AKAP79 (*Figure 1*E & F). Taken together our data therefore indicate that AKAP79 greatly enhances CN activity towards phosphorylated RII subunits at physiological concentrations.
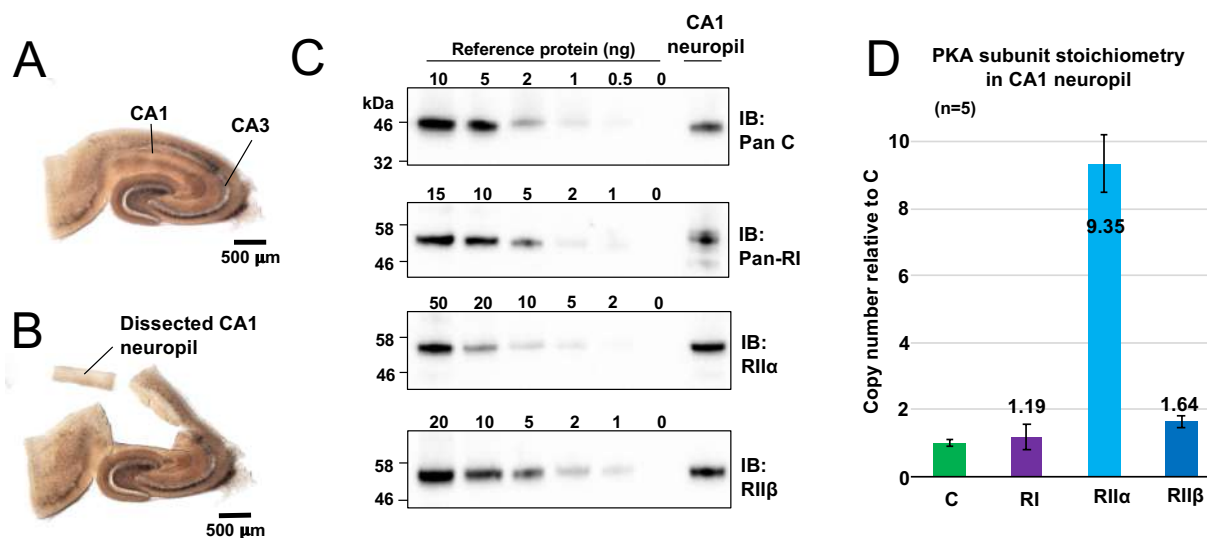

Figure 2. Quantitation of PKA subunits in CA1 neuropil. Images of a P17 rat hippocampal slice before (**A**) and after (**B**) micro-dissection of the CA1 neuropil layer. (**C**) Immunoblots of CA1 neuropil extract for PKA subunits. Extracts were run alongside reference amounts of the relevant purified PKA subunit in each immunoblot (*Figure 2-figure supplement 1*). In each case, 15 µg total protein extract was run alongside the reference series, with the exception of the anti-C immunoblot (10 µg extract). (**D**) Copy numbers of PKA subunits in rat CA1 neuropil normalized to C subunits.

AKAP79 enables calcineurin to suppress type II PKA activity

Given that AKAP79 supports rapid pRII dephosphorylation by CN, we hypothesized that the AKAP could enable CN to directly reduce the fraction of dissociated C subunits in mixtures of RII and C subunits. To test this hypothesis, we utilized purified A-kinase activity reporter 4 (AKAR4) (*Figure 3*A). PKA

6

181   phosphorylation at threonine within the reporter's central 'LRRA**T**LVD' motif leads to a conformational

182   change that increases FRET efficiency between the terminal fluorescent proteins (***Figure 3***A)(Depry et al.,

183   2011). All AKAR4 experiments were performed using purified protein mixtures in 96-well plates. For each

184   recording, three baseline 520/485 nm emission ratios were measured prior to injection of ATP and the

185   desired concentration of cAMP into the protein mixture to initiate phosphorylation. Emission ratios were

186   collected once every 5 seconds (s) thereafter. In calibration experiments with AKAR4 and different

187   concentrations of C subunit only (***Figure 3-figure supplement 1***A), we found that the initial rate of AKAR4

188   phosphorylation had a close to linear relationship to C subunit concentration up to 400 nM C subunit

189   (***Figure 3-figure supplement 1***B). Full AKAR4 phosphorylation increased the emission ratio by 72 %

190   (***Figure 3-figure supplement 1***A), consistent with previous studies (Depry et al., 2011). Importantly,

191   supplementing these reactions with 1.5 μM activated CN had no effect on AKAR4 phosphorylation rates,

192   indicating that the phosphatase cannot directly dephosphorylate the reporter (***Figure 3-figure supplement***

193   ***1***C & D).
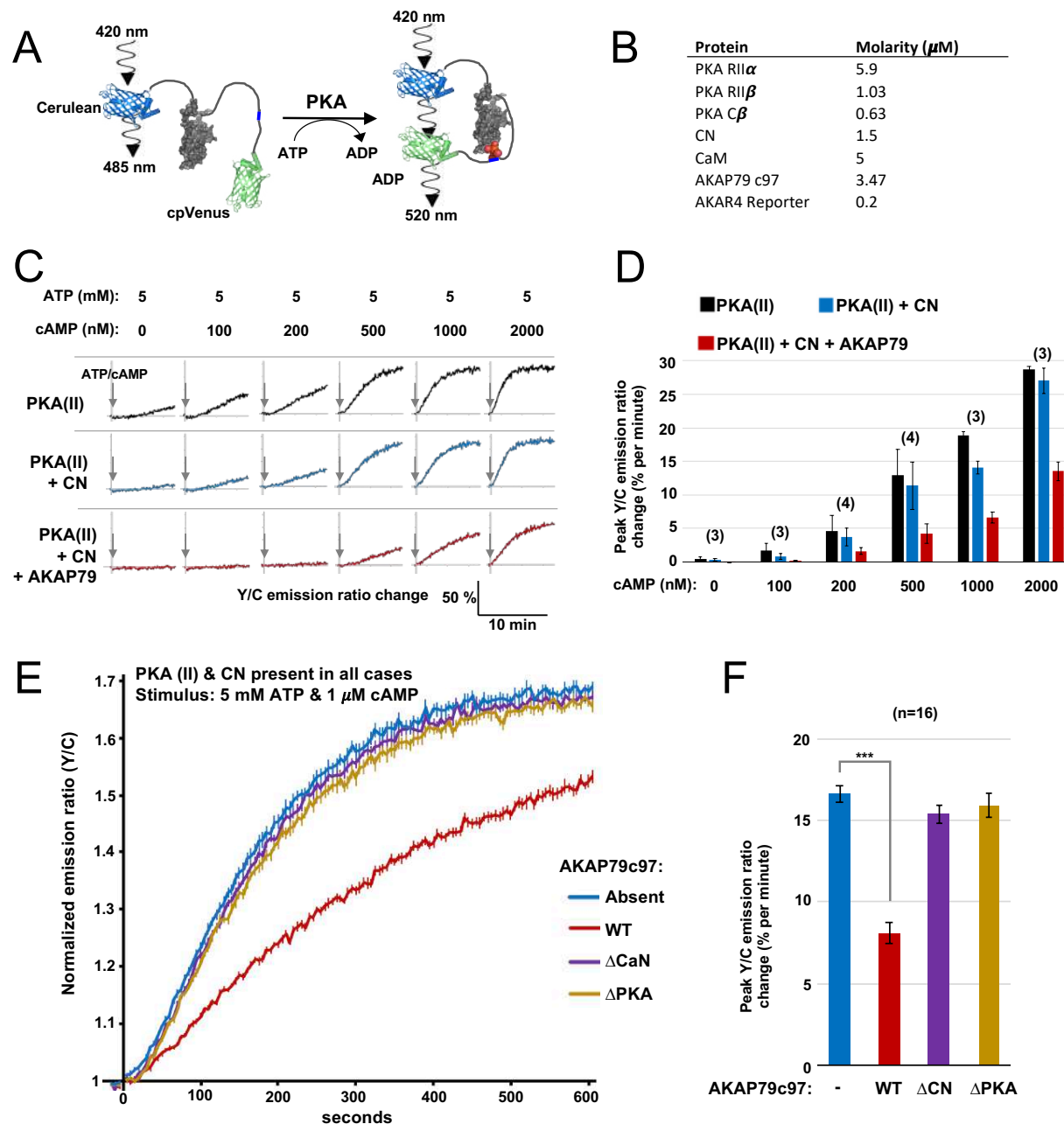
Figure 3. FRET-based PKA activity measurements. (**A**) AKAR4 mechanism: phosphorylation of the sensor by PKA is detected as an increase in FRET between the terminal fluorescent proteins. (**B**) Concentrations of proteins used for *in vitro* AKAR4 assays. Different experiments utilized different mixtures of these proteins but always at these concentrations. (**C**) Representative AKAR4 traces showing change in 520 nm / 485 nm (Y/C) emission ratio over time after injection of different concentrations of cAMP in tandem with 5 mM ATP. All protein mixtures included AKAR4, type II PKA (RIIα, RIIβ, C), and CaM. Experiments were performed with either no further additives (top row, black), with CN added (middle row, blue), or with both CN and AKAP79$_{c97}$ added (bottom row, red). ATP/cAMP injections are indicated by arrows. (**D**) The chart shows peak rates of emission ratio change for the recordings shown in the preceding panel. n values are stated above the columns. (**E**) For these recordings, type II PKA, CN, and CaM were included in all cases. Phosphorylation was

8

205   initiated by injection of 5 mM ATP and 1 μM cAMP at t=0. Averaged responses ± standard error (SE) are

206   shown with no further additives (blue), or when either WT (red), ΔCN (purple), or ΔPKA (gold) variants of

207   AKAP79$_{c97}$ were included. (**F**) Peak rates (calculated between 30-90 s) for the responses shown in the

208   preceding panel. Statistical comparisons were performed using two-tailed unpaired Student *t*-tests.

209   ***p<0.001.

210

211

212   Next, we assembled purified protein mixtures with the aim of mimicking signaling involving PKA, CN,

213   and AKAP79 in CA1 dendritic spines. RIIα, RIIβ, and C subunits were included at concentrations

214   determined in CA1 neuropil extracts (**Figure 2**). CaM was added at a molar excess of 5 μM, CN at 1.5 μM

215   (Goto et al., 1986), and AKAP79$_{c97}$ – when included – at half the concentration of total RII subunits

216   (summarized in *Figure 3*B). RI subunits were omitted since they are not thought to be present in dendritic

217   spines (Ilouz et al., 2017; Tunquist et al., 2008), and because the RI inhibitor site is not phosphorylated so

218   cannot be regulated by CN. We first monitored AKAR4 phosphorylation in reactions containing RIIα, RIIβ,

219   C, and CaM (black, *Figure 3*C). Increasing the concentration of cAMP injected alongside ATP raised rates

220   of AKAR4 phosphorylation as expected (black bars, *Figure 3*D). Supplementing the reactions with CN led

221   to small but consistent decreases in the rate of AKAR4 phosphorylation at all cAMP concentrations (blue,

222   *Figure 3*C & D). Rates were determined between 30-90 s in the linear early phase that followed a brief ~15

223   second delay, with the exception of the lowest two cAMP concentrations (0 & 100 nM), where relatively

224   slow rates were calculated between 30-330 s. Additional supplementation with AKAP79$_{c97}$ markedly

225   decreased the rate of AKAR4 phosphorylation (red, *Figure 3*C). For example, with 1 μM cAMP activation,

226   addition of both CN and the AKAP reduced the initial rate of AKAR4 phosphorylation by 2.8-fold from

227   18.9±0.6 to 6.7±0.8 % per minute (p = 0.0007, black and red bars, *Figure 3*D). To confirm that AKAP79

228   enables CN to suppress PKA activity by anchoring it alongside RII subunits, we investigated the effect of

229   removing either the CN (positions 337-343) or PKA (391-400) anchoring sites. At 1 μM cAMP activation,

230   addition of wild-type (WT) AKAP79$_{c97}$ (red, *Figure 3*E & F) reduced the initial rate of AKAR4

231   phosphorylation by 2.06-fold (p = 2.7 x 10^{-11}) compared to supplementation with only CN (blue). Similar

232   AKAR4 responses were obtained when either the AKAP was omitted altogether (blue, *Figure 3*E & F), or

233   if either the CN (purple) or PKA (orange) anchoring sites in the AKAP were removed. Overall, these

234   AKAR4 measurements reveal that AKAP79 enables CN to robustly decrease type II PKA activity by

235   anchoring the two enzymes together.

236

237   **Mechanistic basis of PKA suppression by calcineurin and AKAP79**

238   We next aimed to quantify how AKAP79 and CN changed the fraction of free C subunits in our reaction

239   mixtures. To estimate this, we cross-referenced rates of AKAR4 phosphorylation recorded in the 'spine

240   mimic' reaction mixtures (*Figure 3*C & E) to the reference curve (r = 0.998) obtained with only C subunits

241   (*Figure 3-figure supplement 1*B). We focused on determining free C subunit concentrations during the

242   early period of linear change (30-90 s for cAMP concentrations of 0.2 μM and above) where we assume

243   the underlying kinetics are close to equilibrium. We calculated free C subunit concentrations following this

244   approach using all available data between 0 to 2 μM cAMP (*Figure 3-figure supplement 1*E). The

245   calculated proportion of C subunits that are dissociated at different cAMP concentrations are shown for

246   type II PKA + CaM either alone (black, *Figure 4*A), with CN (blue, *Figure 4*B), or with both CN and

247   AKAP79$_{c97}$ (red, *Figure 4*C). Together, AKAP79 and CN reduced the proportion of free C subunits at

248   equilibrium across the cAMP concentration range including from 47.8±1.5 to 20.2±0.8 % at 1 μM cAMP,

249   and from 65.7±1.1 to 33.2±3.3 % at 2 μM cAMP (*Figure 4*A & C). The effect of adding CN alone was

250   limited (*Figure 4*B), consistent with the much lower activity of the phosphatase towards pRII subunits in

251   the low micromolar range (*Figure 1*E & F).

252

253   To understand at a deeper level how CN and AKAP79 reduce the fraction of free C subunits, we updated

254   and extended a kinetic model (Buxbaum & Dudai, 1989) that takes into account transitions between pRII

255   (left-hand square, *Figure 4*D) and unphosphorylated RII subunits (right-hand square). The extended model

256   also incorporates AKAR4 binding to and phosphorylation by free C subunits. We used a Bayesian approach

257   (Eriksson et al., 2019) to estimate parameter sets for the model that could fit data pooled from AKAR4

258   recordings obtained after stimulation with 1 and 2 μM cAMP (*Figure 3*C & E). A log uniform prior

259   parameter distribution was used as a starting point for the Bayesian method, with the bounds of each

260   parameter set according to empirical data (*Supplementary Table 1*), including rates of pRII

261   dephosphorylation determined in this study (*Figure 1*), and binding rates of C subunits to pRII and RII

262   (Zhang et al., 2015). This approach was terminated after identifying approximately 10,000 parameter sets

263   that could explain the experimental data (*Figure 4*E-G). Simulations using these parameter sets capture the

264   initial delay that occurs in the first ~ 15 s since all reactions initially start with dephosphorylated RII

265   subunits (e.g., grey lines, *Figure 4*E), and they enabled us to predict concentration changes of individual

266   states within the model that cannot be determined experimentally (first three columns, *Figure 4-figure*

267   *supplement 1*). The model indicates that AKAP79 and CN together shift C subunit capture to the faster

268   right-hand square sub-system (*Figure 4*D), driving down the fraction of free C subunits and thereby

269   reducing PKA activity.

270
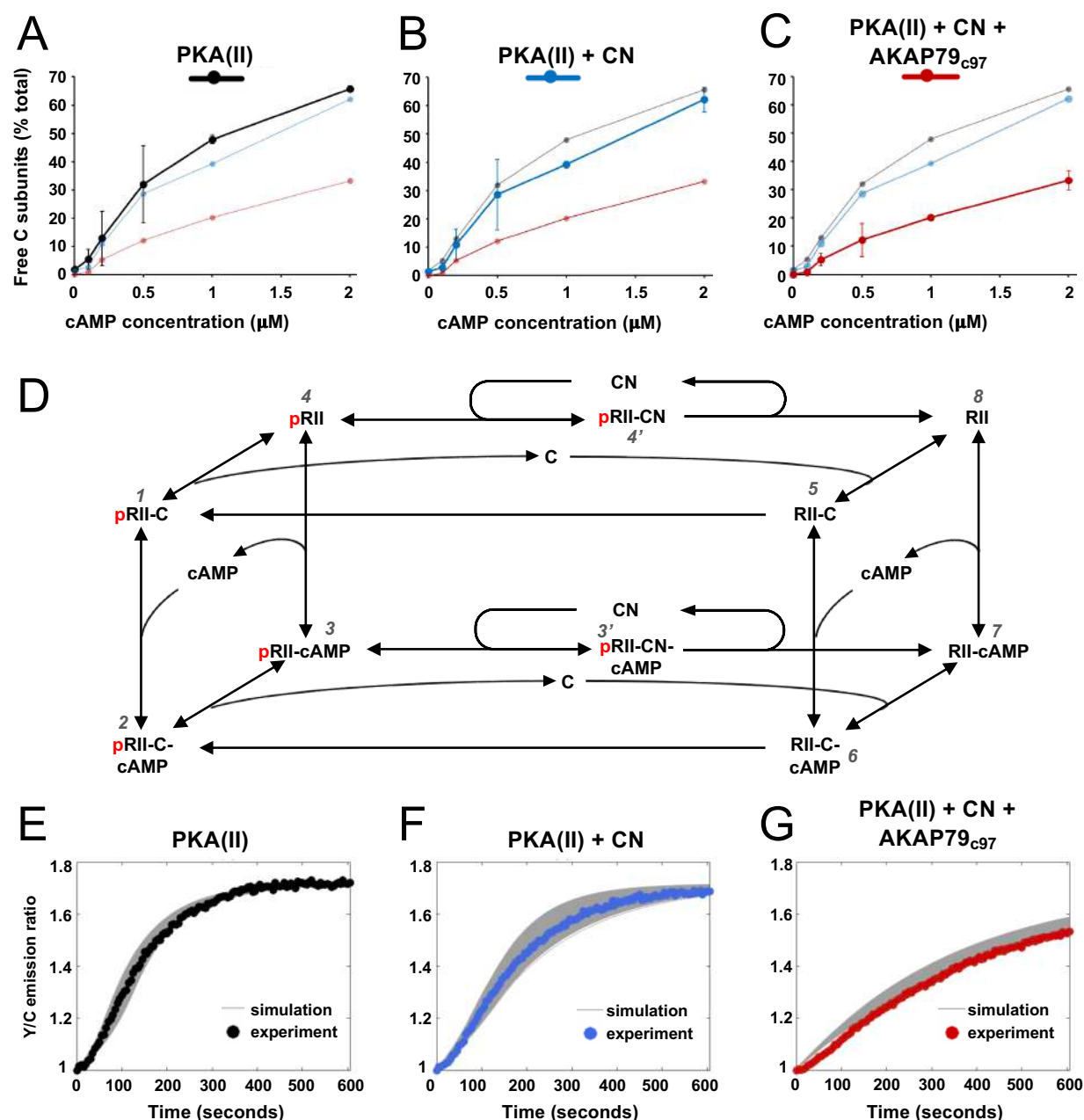
Figure 4. Kinetic analysis of PKA-CN-AKAP79 signaling. (**A-C**) Estimates of the average proportion of free C subunits between 30-90 s for type II PKA alone (black), with CN (blue), and with both CN and AKAP79$_{c97}$ (red) following activation of the protein mixtures with a range of cAMP concentrations. (**D**) Reaction scheme used for modeling type II PKA regulation by CN. Each species within the scheme is numbered consistent with supporting data in figure in ***Supplementary Table 1***. (**E-G**) Model simulations for protein mixtures activated with 1 μM cAMP are shown with the experimental data overlaid. Averaged values are shown for experimental data after pooling the data shown in ***Figure 3***. Responses are shown for type II PKA alone (**E**), with CN (**F**), and with both CN and AKAP79$_{c97}$ (**G**). A sample of the corresponding simulated responses are shown in grey. An 'error' threshold of 0.01 was used to accept curves as a good fit.

11

Mutation of the RIIα IS phosphorylation site occludes PKA suppression by CN

The results of the preceding sections show that AKAP79 targeting of CN for direct suppression of PKA is a viable mechanism for LTD induction. Previously published studies in hippocampal slices involving genetic manipulation of AKAP150 (the rodent ortholog of AKAP79) are also consistent with this mechanism. Full AKAP150 knock-out (Lu et al., 2008; Tunquist et al., 2008; Weisenhaus et al., 2010), or AKAP150 knock-in with variants lacking either the PKA or CN anchoring sites (Jurado et al., 2010; Sanderson et al., 2016), show that both AKAP150 anchoring sites are required for LTD induction. However, such approaches cannot distinguish between CN targeting to pRII subunits versus other substrates. If direct suppression of PKA activity by CN is essential for LTD induction, we reasoned that mutation of the IS phospho-acceptor S98 (*Figure 5*A) in the predominant RIIα isoform would be expected to disrupt LTD induction in CA1 neurons. To confirm this presupposition before undertaking experiments in neurons, we re-ran AKAR4 experiments at 1 μM cAMP substituting in either S98A or S98E RIIα. For each RIIα variant (*Figure 1-figure supplement 1*H), we compared responses with or without CN, with WT RIIβ and AKAP79$_{c97}$ present in all cases. For WT RIIα, addition of CN to the mixture decreased the peak rate of AKAR4 phosphorylation from 21.02±0.76 (light blue, *Figure 5*B) to 8.24±0.79 % per minute (dark blue). Substituting in RIIα S98A generated slow rates of AKAR4 phosphorylation in both cases (6.30±0.44 % per min with CN, and 6.67±0.56 % without, *Figure 5*C). Conversely, the peak rate of AKAR4 phosphorylation was high regardless of the presence of CN for the S98E RIIα variant (31.30±3.60 % per min without CN; 25.65±3.44 % with CN, *Figure 5*D). Together, this data indicates that substituting in either mutant of RIIα in neurons would be expected to reduce LTD induction in neurons if direct suppression of PKA by CN is required in LTD induction (*Figure 5*E).
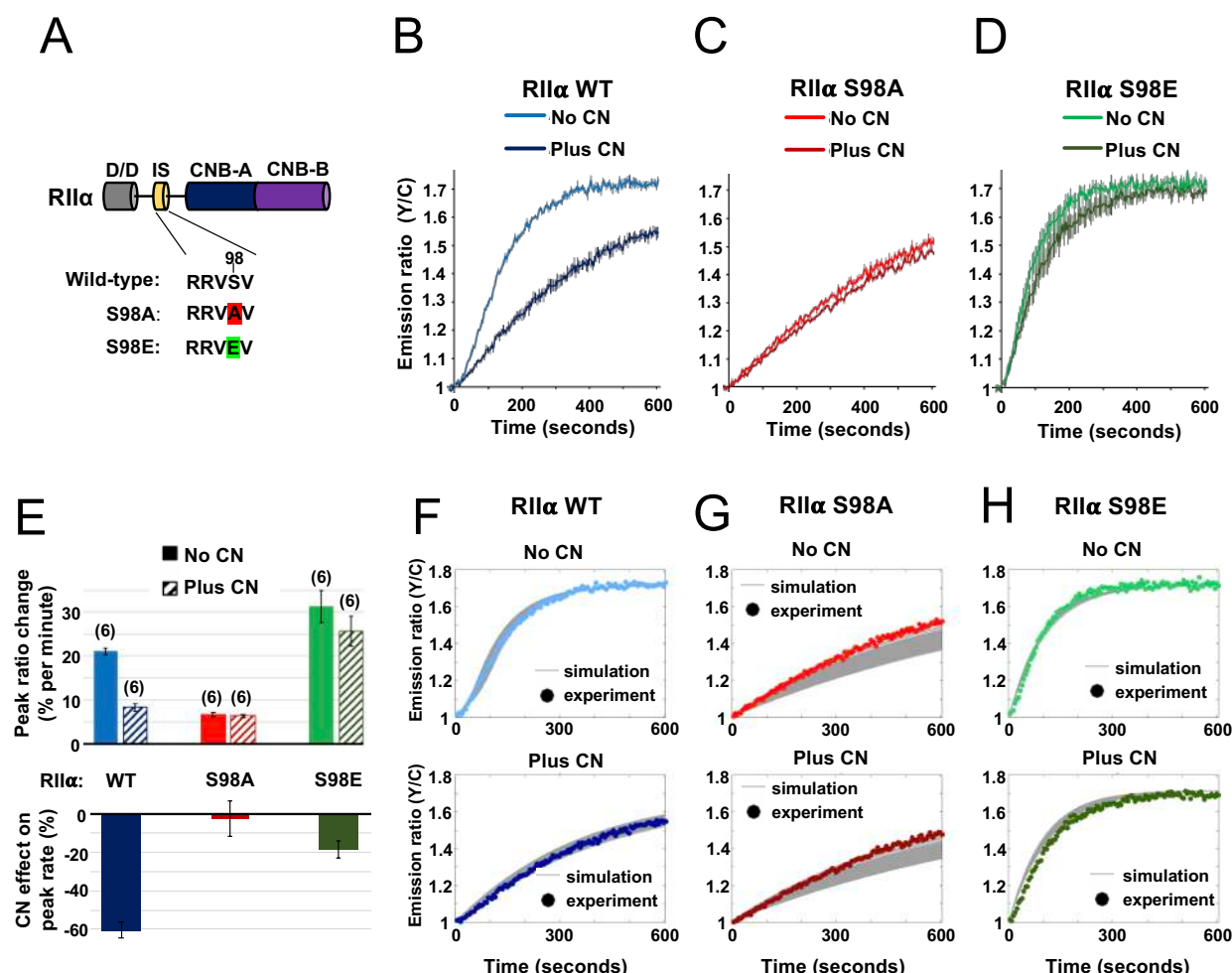
Figure 5. Characterization of RIIα IS phosphorylation site mutations. (**A**) RIIα subunit topology showing locations of the docking and dimerization domain (D/D, grey), inhibitor sequence (IS, yellow), and tandem cyclic nucleotide binding domains (dark and light blue). S98A (red) and S98E (green) mutations in the IS are highlighted. (**B-D**) Comparison of AKAR4 emission ratio changes following 5 mM ATP/1 µM cAMP activation of protein mixtures containing either WT (**B**), S98A (**C**), or S98E (**D**) RIIα. 1.03 µM RIIβ was included in all cases. Measurements were collected either with or without CN in the reaction mixture. Averaged responses (± SE) are shown for WT RIIα with (dark blue) and without CN (light blue), S98A RIIα with (dark red) and without (light red) CN, and RIIα S98E with (dark green) and without (light green) CN. (**E**) The upper bar chart shows peak rates (calculated between 30-90 s) for the responses shown in panels b-d. The effect of including CN in the reaction mixture for each RII variant is shown in the lower bar chart. (**F-H**) Model predictions in the six conditions of panels b-d are shown in grey when simulating using the 'extended' model (see Methods) and using the different parameter sets generated from the parameter estimation approach. The same parameters as retrieved using data shown in figure 4 were used as a starting point for the simulations, but parameter sets were filtered based on data collected with RIIα S98A. Model predictions are shown alongside the corresponding experimental data collected with either WT (**F**), S98A (**G**), or S98E (**H**) RIIα in the reaction mix.

13

322

323   Before moving on to experiments in neurons, we used the data collected with RIIα variants to test the

324   accuracy of our kinetic modeling. We ran simulations assuming that the S98A and S98E variants of RIIα

325   would behave like dephosphorylated and phosphorylated forms of the regulatory subunit. Broadly, the

326   simulations were in line with our experimental data and predicted that addition of CN would reduce PKA

327   activity substantially more in the WT but not RIIα mutant conditions (***Figure 4-figure supplement 1***), with

328   low and high PKA activities regardless of CN concentration for the S98A and S98E variants, respectively.

329   The model predictions for the extent by which AKAR4 phosphorylation was depressed in the RIIα S98A

330   system were, however, spread out depending on the specific parameter set (column 4-5, ***Figure 4-figure***

331   ***supplement 1***). This implies that the WT data we used to constrain the model were not sufficient to precisely

332   constrain the dynamics specifically for the unphosphorylated RII sub-system (right square, ***Figure 4***D) To

333   understand the characteristics of those parameter sets that also reproduced the RIIα S98A behavior, we

334   filtered the parameter sets returned by the parameter estimation approach into two classes depending on

335   whether they fit closely (blue, ***Figure 4-figure supplement 1***) or not (red) to the acquired mutation data,

336   yielding 422 parameter sets that fit closely to both the WT and mutation data. A pairwise coordinate plot

337   (see ***Figure 5-figure supplement 1***A) shows that, overall, the two classes of parameter sets do not appear

338   to be visually distinct with regards to kinetic rates. However, analysis and subdivision of the eight model

339   dissociation constants (K_D's) reveals an interesting relation among them (***Figure 5-figure supplement 1***B).

340   As shown by the scatterplots for the K_D for interaction between RII-C and cAMP (K_D56) and RII-cAMP

341   and C (K_D76) (***Figure 5-figure supplement 1***C), K_D56 should be relatively low within its range paired with

342   a relatively high K_D76 (***Figure 5-figure supplement 1***D) to accurately mimic the biological workings of

343   the PKA sub-system. This pairing ensures that sufficient C subunit is released by cAMP when the kinetics

344   are restrained to the unphosphorylated RII sub-system when the RIIα S98A mutation is introduced. Overall,

345   simulations using unfiltered (top row, ***Figure 4-figure supplement 1***) and filtered (***Figure 5***F-H) parameter

346   sets show that the kinetic model closely reproduces the experimental data, especially when further

347   constrained using data collected with RIIα S98A. Taken together, experiments and simulations with S98A

348   and S98E variants of RIIα show that either of these mutations should prevent AKAP79 and CN from

349   switching C subunit capture from the left-hand square sub-system to the faster right-hand square (***Figure***

350   ***4***D). Therefore, either substitution would be expected to reduce LTD induction if the mechanism is

351   important *in vivo*.

352

353   **Disruption of RIIα phosphorylation in CA1 neurons impedes chemical LTD**

354   To enable neuronal RIIα replacement experiments, we generated lentiviruses for shRNA-mediated

355   knockdown of endogenous RIIα and simultaneous expression of shRNA-resistant RIIα variants in tandem

14

356   with GFP. The lentiviruses contain an H1 promoter for expression of a highly-effective shRNA targeted to

357   RIIα (*Figure 6*A). A UbC promoter drives expression of replacement RIIα sequences in tandem with GFP,

358   with an internal ribosome entry sequence (IRES2) between the coding sequences of the two proteins

359   enabling expression of GFP. We validated the lentiviruses in dissociated rat primary hippocampal neurons

360   by comparing the efficacy of five different lentiviruses. On day 7 *in vitro* (DIV7), we infected with control

361   lentiviruses expressing either scrambled or shRIIα RNA, or with complete viruses for replacement of

362   endogenous RIIα with either WT, S97A, or S97E (RIIα in rat is equivalent to S98 in human RIIα). Neuronal

363   protein extracts were collected on DIV14, and analyzed using immunoblotting. Anti-RIIα immunoblotting

364   (top row, *Figure 6*B) confirmed effective suppression of endogenous RIIα with shRIIα (lane 3) but not

365   scrambled RNA (lane 2), and strong expression of the replacement sequences (lanes 4-6). Expression of

366   PKA C (row 2, *Figure 6*B) and RIIβ subunits (row 3) was not affected by lentiviral infection in any case.

367   Blocking PKA activity with H89 is known to prevent growth of new spines, whereas stimulating PKA with

368   forskolin increases spine formation (Kwon & Sabatini, 2011). Replacing RIIα with the S97A variant –

369   which has lower PKA activity regardless of CN activity (*Figure 5*F) – would therefore be expected to lead

370   to a reduction in spines. To test this, we imaged dendritic spines on primary hippocampal neurons

371   expressing either WT (left panel, *Figure 6*C), S97A (middle panel), or S97E (right panel) RIIα. Consistent

372   with a role for PKA in spinogenesis, spine density was reduced by 33.5 % (p=0.002) in neurons expressing

373   the S97A variant to 1.17±0.11 spines per 10 μm compared to 1.76±0.12 for WT RIIα. Spine density for the

374   S97E variant was similar to WT at 1.86±0.11 spines/10 μm.

375

376   To test whether the two substitutions at RIIα S97 affect LTD, we monitored changes in dendritic spine

377   number during chemical LTD – a model of long-term synaptic depression that can be applied in dissociated

378   neuronal cultures. Bath application of 20 μM NMDA for 3 minutes triggered a steady reduction in spine

379   density (*Figure 6*E, top row) in neurons expressing WT RIIα as expected (Zhou et al., 2004), reaching a

380   20.4±1.6 %% reduction in spines after one hour (blue, *Figure 6*F). In comparison, spine loss was attenuated

381   in neurons expressing either the S97A (*Figure 6*E, middle row) or S97E (bottom row) RIIα variants. Spine

382   numbers were reduced by only 9.07±0.96 % in neurons expressing RIIα S97A (red line, *Figure 6*F), and

383   by 9.90±1.8 % for the S97E variant (green line). The residual LTD in both conditions may correspond to

384   action of CN on substrates other than pRII subunits, and limited suppression of PKA activity through CN

385   dephosphorylation of the relatively small number of WT RIIβ subunits that are present in all cases. Overall,

386   attenuation of spine loss in neurons expressing either S97A (p=0.00046) and S97E (p=0.0014) RIIα

387   compared to WT subunits is consistent with an important role for direct PKA activity suppression by CN

388   during the induction of LTD.

389
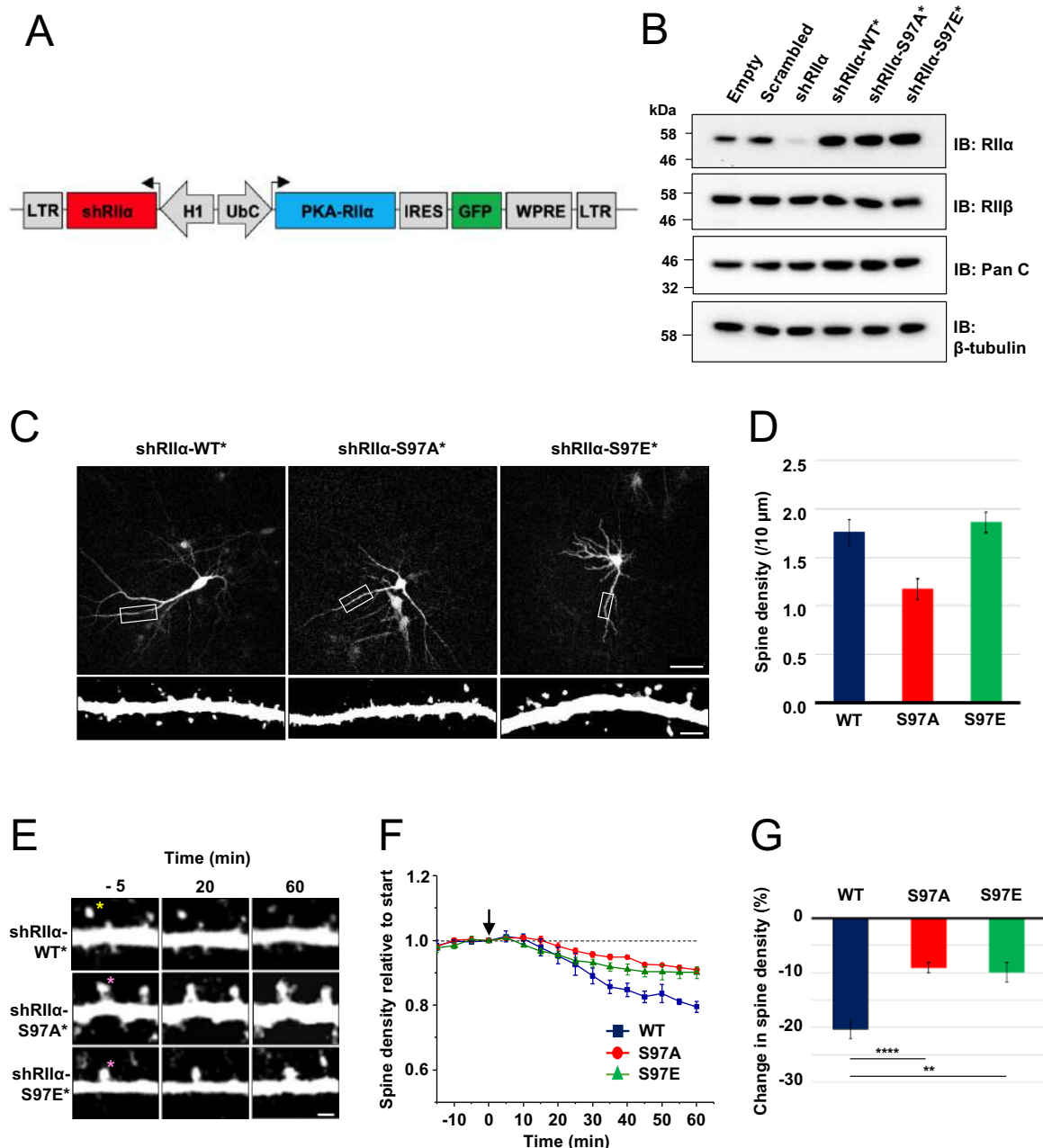
390
391 **Figure 6. Lentivirus development and spine density imaging.** (**A**) Schematic of the FUGW-H1-based
392 lentiviral vector used to knock down and replace endogenous RIIα subunits in dissociated hippocampal
393 cultures. (**B**) To validate lentiviruses, dissociated hippocampal neurons were infected on the seventh day *in*
394 *vitro* (DIV7). Immunoblots are shown comparing neuronal extracts collected on DIV14 after infection with no
395 virus, virus expressing scrambled shRNA only, shRIIα only, and the three complete lentiviruses for
396 knockdown/replacement with either WT, S97A, or S97E RIIα. (**C**) Representative live-cell images of
397 lentivirus-infected primary hippocampal neurons at DIV14 expressing either WT, S97A, or S97E RIIα. Scale
398 bars correspond to 50 μm (upper panels) and 5 μm (lower panels). (**D**) Average spine density on hippocampal
399 dendrites following lentiviral replacement of endogenous RIIα. Data were averaged from 106 (WT), 97 (S97A),
400 and 113 (S97E) neurons derived from 7 rats for each condition, and are represented as mean ± SE. Conditions

16

401   were compared using one-way ANOVA with Turkey post-hoc tests. (**E**) Representative live-cell images
402   showing dendritic spines in primary hippocampal neurons expressing either WT, S97A, or S97E replacement
403   RIIα at three points before and after chem-LTD (scale bar = 2.5 μm). Chem-LTD was induced at t=0 with 20
404   μM NMDA for 3 minutes. The yellow asterisk indicates a spine that disappeared over the course of the protocol
405   whereas the pink asterisks indicate spines that did not. (**F**) Plot showing average changes in spine density (±
406   S.E) in primary hippocampal neurons expressing either WT (dark blue), S97A (red) or S97E (green) RIIα. (**G**)
407   Average changes in spine density ± SE one hour after induction of chem-LTD are shown for neurons expressing
408   WT (dark blue, n=5), S97A (red, n=5), and S97E (green, n=4) RIIα variants as shown in the preceding two
409   panels. Statistical comparisons were performed by 2-way ANOVA followed by Bonferroni's post-hoc test.
410   **$p<0.01$, ***$P<0.001$

411

412

Discussion

414

415   The observations in this study support a revised mechanism for CN-mediated long-term depression in CA1
416   model synapses. AKAP79/150 is critical for anchoring PKA in dendritic spines (Tunquist et al., 2008;
417   Weisenhaus et al., 2010) through association with RII subunits, which are the predominant neuronal PKA
418   subunit in ~11-fold molar excess of C subunits in the CA1 neuropil (**Figure 2**D). Imaging studies(Ilouz et
419   al., 2017; Weisenhaus et al., 2010) are consistent with our quantitative immunoblotting data, which show
420   that RIIα is the major RII isoform in the CA1 neuropil. pRII dephosphorylation is limited prior to Ca^{2+}
421   stimulation (**Figure 7**A), enabling a tonic level of dissociated C subunits sufficient to basally phosphorylate
422   postsynaptic substrates in dendritic spines such as GluA1 subunits of AMPA-type glutamate
423   receptors(Bear, 2003). LTD is brought about by CN (Mulkey et al., 1994), which is activated by Ca^{2+}
424   entering spines through NMDA-type glutamate receptors (**Figure 7**B). AKAP79/150 contains a 'PIAIIIT'
425   CN anchoring motif that is necessary for LTD (Jurado et al., 2010; Sanderson et al., 2012). In addition to
426   potentially targeting CN to postsynaptic substrates including GluA1 subunits, the PIAIIIT anchoring motif
427   positions CN adjacent to pRII subunits where it can efficiently dephosphorylate them (**Figure 7**B). This
428   enables CN to increase the concentration of dephosphorylated RII species (blue spheres in the kinetic
429   scheme shown in **Figure 7**B) thereby directly suppressing PKA activity by increasing the rate of PKA C
430   subunit capture. Consistent with this mechanism, blocking regulation of RII phosphorylation state by
431   introducing mutations that mimic either the phosphorylated or dephosphorylated forms of the IS reduces
432   LTD in cultured hippocampal neurons.

433

434   Our discovery that CN can directly suppress PKA activity in the AKAP79 complex reconciles three aspects
435   of AKAP79 structure and function that had been enigmatic and paradoxical. First, previous studies showed
436   that AKAP79 acts as a weak inhibitor of CN towards peptide substrates including a 20-mer peptide

437   encompassing the phosphorylated RII IS (Coghlan et al., 1995; Kashishian et al., 1998), apparently at odds

438   with the functional requirement for the anchoring protein in targeting CN to bring about LTD. We show

439   that the key substrate for CN is likely to be full-length pRII subunits, and that in fact AKAP79 enhances

440   the activity towards pRII at physiological concentrations by more than ten-fold. A second enigmatic feature

441   of AKAP79 is its CN anchoring motif, PIAIIIT, which includes an additional central residue compared to

442   the typical PxIxIT motif (Roy & Cyert, 2009). In a crystal structure of CN in complex with a peptide

443   corresponding to AKAP79 positions 336-346, the additional leucine supports simultaneous binding of two

444   copies of CN on either side of the motif (Li et al., 2012). Native mass spectrometry measurements of a

445   purified AKAP79-CN-CaM-RIIα D/D complex also support a stoichiometry of 2 CN to 1 AKAP79 (Gold

446   et al., 2011), although solution measurements indicate that when full-length RII subunits are bound to

447   AKAP79, only one copy of CN can bind at a time(Li et al., 2012; Nygren et al., 2017). One possible

448   explanation for this behavior is that CN binds transiently to either side of the AKAP79 PIAIIIT motif

449   enabling it to access both protomers of RII anchored to AKAP79 for efficient pRII dephosphorylation

450   (cartoon representations in *Figure 7*). This idea is consistent with data showing that mutating the PIAIIIT

451   motif to a high-affinity canonical PxIxIT motif impairs the function of the phosphatas (Li et al., 2012).

452   Third, existing models of AKAP79 function assume that CN anchored to AKAP79 overcomes PKA

453   phosphorylation at substrates with no reduction in PKA phosphorylation rate. In our revised mechanism,

454   CN directly suppresses PKA activity when removing phosphate from substrates primed by PKA thereby

455   avoiding energetically-costly ongoing futile cycling of phosphorylation and dephosphorylation by PKA and

456   CN at these sites.

457

458
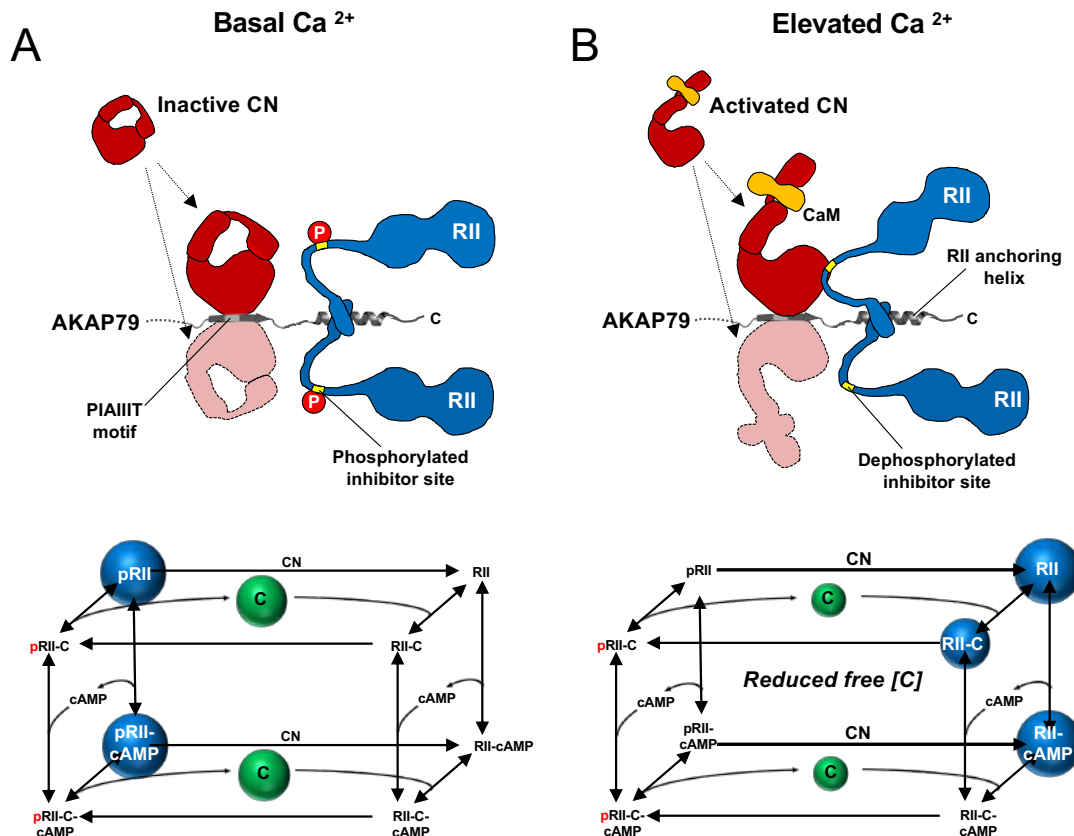
Figure 7. Summary model of PKA suppression by CN within the AKAP79 complex. Structural and kinetic models (upper and lower panels, respectively) of signaling within the AKAP79 complex are shown under conditions of either low (**A**) or elevated Ca^{2+} (**B**). Elevated Ca^{2+} triggers CN (red) dephosphorylation of pRII (blue) which shifts C subunit capture from the left-hand square of the kinetic scheme to the right-hand square which features dephosphorylated forms of RII. The overall effect is a reduction in the concentration of free C subunits. The most abundant forms of RII under the two conditions are highlighted by blue spheres.

A challenge in the future will be to understand how the mechanism uncovered here relates to the full complexity of AKAP79 function. AKAP79 is directly regulated by Ca^{2+}/CaM, which binds to a 1-4-7-8 hydrophobic motif (Patel et al., 2017) starting at position W79. Binding of Ca^{2+}/CaM releases AKAP79 from the postsynaptic membrane (Dell'Acqua et al., 1998) and alters the conformation of the signaling complex by triggering formation of a second interface between CN and AKAP79 that involves an LxVP-type motif in AKAP79 (Gold et al., 2011; Nygren et al., 2017). It will be important to understand how this Ca^{2+}-sensitive interface affects CN suppression of PKA activity. Localization of AKAP79 is also regulated by palmitoylation at C36 and C139 (Delint-Ramirez et al., 2011; Keith et al., 2012). Palmitoylation is required for endosomal localization of AKAP79, and AKAP79 depalmitoylation and synaptic removal is additionally regulated by CaMKII (Woolfrey et al., 2018). Our work suggests that removal of AKAP79

19

478   from synapses might be synchronized with accumulation of inhibited C subunits in the AKAP79 complex.

479   AKAP79 is a highly multivalent protein – other notable documented interaction partners include protein

480   kinase C (Hoshi et al., 2010) and the Ca^{2+}-activated cyclase AC8 (Baldwin & Dessauer, 2018; Zhang et al.,

481   2019). Oscillations of Ca^{2+}, cAMP, and PKA activity have been observed in pancreatic β-cells (Hinke et

482   al., 2012; Ni et al., 2011), and knockout of AKAP150 leads to the loss of cAMP oscillations in β-cells upon

483   stimulation with insulin (Hinke et al., 2012). CN dephosphorylation of pRII subunits bound to AKAP79 is

484   likely to play a role in oscillatory patterns of PKA activity, and it will be important to understand how this

485   mechanism underlies responses to short-lived and oscillatory changes in Ca^{2+} and cAMP concentration.

486

487   In this combined experimental-computational study, we focused on AKAP79 signaling in dendritic spines

488   on the basis that this could serve as a prototype for understanding a potentially widespread non-canonical

489   mechanism for altering PKA. In addition to its role in dendritic spines, AKAP79 regulates many different

490   membrane channels and receptors following Ca^{2+} influx through a variety of sources, and the mechanism

491   that we have uncovered here is likely to at least extend to these additional contexts. For example, AKAP79

492   underlies GABA$_A$ receptor regulation during LTD of GABAergic synapses (Dacher et al., 2013), and it

493   positions PKA and CN for regulation of TRPV channels (Zhang et al., 2008), Kv7 channels (Zhang &

494   Shapiro, 2012), and both β-adrenergic receptor isoform (Houslay & Baillie, 2005). AKAP79 is also

495   necessary for NFAT dephosphorylation following Ca^{2+} entry through both L-type calcium channels (Wild

496   et al., 2019) and the store-operated Ca^{2+} channel ORAI1 (Kar et al., 2014). The RII IS phosphorylation site

497   is conserved throughout the animal kingdom, and co-anchoring of phosphatases alongside PKA is a feature

498   of several AKAP complexes (Redden & Dodge-Kafka, 2011). Future investigations may therefore explore

499   whether additional anchoring proteins are able to direct CN – or other cellular phosphatases – for direct

500   suppression of PKA activity.

Methods & Materials

Protein expression and purification. Human PKA subunits were expressed and purified as described previously (Walker-Gray et al., 2017). GST-RIIα and GST-RIIβ were expressed in *Escherichia coli* BL21 Tuner (DE3) pLysS, and GST-Cβ in *E. coli* BL21 (DE3) grown in LB. In all cases, protein expression was induced by addition of 0.5 mM isopropyl β-D-1-thiogalactopyranoside (IPTG), and bacteria were harvested following overnight incubation at 20 °C. Cell pellets were thawed and sonicated in glutathione sepharose binding buffer (20 mM HEPES pH 7.5, 500 mM NaCl, 1 mM DTT, 0.5 mM EDTA, 1 mM benzamidine, 10 % glycerol) supplemented with 0.1 mg/mL lysozyme, and 0.1 % Igepal CA-630 (RII subunit preps only). Clarified lysates were incubated with glutathione sepharose 4B, and PKA subunits were eluted by overnight cleavage with PreScission protease thus removing N-terminal GST affinity tags. Finally, each subunit was purified using a HiLoad 16/600 Superdex 200 column connected in series with a GSTrap to remove residual GST using gel filtration buffer (20 mM HEPES pH 7.5, 150 mM NaCl, 5 % glycerol). S98A and S98E point mutations were introduced into RIIα subunits by site-directed mutagenesis (SDM) with primer pairs hS98A_F & R, and hS98E_F & R. RIIα variants were expressed and purified in the same way as the WT sequences.

Full-length human AKAP79 was cloned into pET28 using primers Nde1_AKAP79_1 and AKAP79_427_EcoRI for expression of N-terminally 6His-tagged protein. AKAP79 was expressed in 4 L BL21 Star (DE3) cells by overnight incubation at 37 °C in auto-induction media (AIM). PBS-washed bacterial pellets were resuspended in Talon binding buffer (30 mM Tris pH 8.0, 500 mM NaCl, 10 mM imidazole, 1 mM benzamidine) supplemented with 0.1 mg/mL lysozyme and one Complete EDTA-free protease inhibitor tablet (Roche) per 100 mL. Lysates were sonicated, clarified by centrifugation, and incubated with Talon Superflow resin for 2 hours prior to 3 x 10 mL washing in Talon binding buffer, and eluted with 2 x 2.5 mL Talon elution buffer (30 mM Tris, pH 7.0, 500 mM NaCl, 300 mM imidazole, 1 mM benzamidine). Eluted protein was exchanged into Q buffer A (20 mM Tris pH 8, 20 mM NaCl, 1 mM EDTA, 2 mM DTT) using a HiPrep 26/10 desalting column to enable purification using a 1 mL Resource Q column. Each variant was eluted using a NaCl/pH gradient with Q buffer A and a steadily increasing proportion of Q buffer B (20 mM Tris pH 7, 500 mM NaCl, 1 mM EDTA, 2mM DTT). In the final step, peak fractions were pooled and buffer exchanged into gel filtration buffer. Residues 331-427 of AKAP79 were cloned into pET28 using primers Nde1_AKAP79_331 and AKAP79_427_EcoRI for expression of the fragment AKAP79$_{c97}$ bearing an N-terminal His tag. This construct was transformed into BL21 (DE3) cells, which were grown overnight at 37 °C in AIM. Lysis and metal affinity steps were as for full-length AKAP79 with the exception that Ni-NTA agarose (Life Technologies) was used in place of Talon resin. Following elution from Ni-NTA resin, the protein was purified by size exclusion using a HiLoad

535   16/600Superdex 200 pre-equilibrated in gel filtration buffer. To assemble complexes of full-length RII

536   subunits and AKAP79$_{c97}$, mixtures of the purified proteins were incubated on ice in gel filtration buffer for

537   1 h with the AKAP fragment in a 2:1 molar excess. The complex was then separated from excess

538   AKAP79$_{c97}$ by Superdex 200 size exclusion. pET28-AKAP79$_{c97}$ ΔCN was generated by performing PCR

539   with an earlier construct lacking residues 337-343 as the template (Gold et al., 2011), whereas the ΔPKA

540   variant (lacking residues 391-400) was generated by SDM with primers ΔPKA_F & _R. The two

541   AKAP79$_{c97}$ deletion mutants were expressed and purified in the same way as the WT protein.

542   Human CN was expressed from a bicistronic pGEX6P1 vector (Gold et al., 2011) in *E. coli* BL21

543   Tuner (DE3) pLysS cells. Protein expression was induced by overnight incubation at 37 °C in 4L AIM. CN

544   was purified following the same protocol as full-length PKA RII subunits, with the final size exclusion step

545   performed using gel filtration buffer supplemented with 1 mM DTT. Human CaM was expressed and

546   purified as described previously (Patel et al., 2017). Briefly, untagged CaM was expressed in *E. coli* BL21

547   (DE3) cells incubated overnight at 37 °C in AIM. CaM was initially purified using phenyl sepharose resin,

548   then by ion exchange with a HiTrap Q HP column. Finally, CaM was exchanged into water and lyophilized

549   prior to storage at -80 ºC. For AKAR4 purification, an 8His epitope tag was ligated into pcDNA3.1-

550   AKAR4-NES vector (Depry et al., 2011) (Addgene cat no. 64727) at the C-terminus of the sensor

551   immediately prior to the nuclear export site using primers EcoI_8HisNLS_XbaI and

552   XbaI_8HisNLS_EcoRI. The vector was transfected into 20 x 10 cm dishes of HEK293T cells cultured in

553   DMEM using lipofectamine-2000 (Thermo Fisher Scientific). Cells were collected after 3 days, washed in

554   PBS, then lysed in Talon binding buffer supplemented with 0.5 % Igepal CA-630, and sonicated briefly.

555   AKAR4 was purified by affinity to Ni-NTA agarose following the same procedure as for AKAP79, and

556   eluted protein was exchanged into gel filtration buffer, and aliquoted before storage at -80 ºC. All

557   purification columns and resins were purchased from GE Healthcare. All protein samples were concentrated

558   using Vivaspin centrifugal concentrators (Sartorius). Denaturing gel electrophoresis was performed using

559   NuPAGE 4-12 % Bis-Tris gels (Thermo Fisher Scientific), and protein concentrations were determined

560   using the bicinchoninic acid (BCA) assay.

561

562   **Phosphatase assays**. CN substrates were prepared by phosphorylating PKA RII subunits at the

563   autoinhibitory site with PKA C subunit and ATP(γ-^{32}P). To radiolabel RIIα, RIIβ, or the purified complexes

564   of each isoform with AKAP79$_{c97}$, 50 μg of the relevant sample was incubated in 100 μL with

565   phosphorylation buffer (20 mM HEPES pH 7.5, 150 mM NaCl, 100 μM cAMP, 5 mM MgCl$_2$, 0.03 μg/μL

566   C subunit) supplemented with 42 pmol [^{32}P-γ]-ATP at 3000 Ci/mmol and 10 μM cold ATP. After 15 min

567   incubation at 30 °C, reactions were supplemented with 10 μM additional cold ATP. Following 15 min

568   further incubation, reactions were finally supplemented up to 1 mM cold ATP for 10 min further incubation.

22

569   ^{32}P-labelled protein was immediately separated from free ^{32}P using Sephadex G-25 Medium equilibrated in

570   phospho-substrate storage buffer (20 mM HEPES pH 7.5, 150 mM NaCl, 10 % glycerol, 0.1 mM EDTA).

571   Additional cold phospho-labelled substrates were prepared using scaled-up reactions with 1 mM cold ATP

572   for 30 min at 30 °C.

573   Phosphatase assays (final volume 50 μL per assay) were prepared by first mixing appropriate

574   dilutions of pRII substrates and CN on ice in dilution buffer (25 mM Na HEPES pH 7.5, 150 mM NaCl) to

575   a final volume of 35 μL. 10 μL of reaction buffer (25 mM Na HEPES pH 7.5, 150 mM NaCl, 25 mM

576   MgCl$_2$, 5 mM DTT, 0.5 mg/mL BSA, 1 mM EDTA) was then added before initiation of CN activity by

577   addition of 5 μL activator mix (25 mM Na HEPES pH 7.5, 150 mM NaCl, 10 mM CaCl$_2$, 50 μM CaM).

578   Assays was terminated after 30-60 s at 30 °C by addition of 350 μL 30 % trichloroacetic acid (TCA).

579   Samples were then incubated on ice for 1 h, and protein was pelleted by centrifugation at 31,360 × g for 15

580   min at 2 °C. The separated supernatant and pellet were analyzed using a Beckman LS 6000SC scintillation

581   counter to determine the fraction of phosphate released from the pRII substrate. Reaction conditions were

582   optimized so that less than 10 % pRII was dephosphorylated in each assay. Assays were generally

583   performed with 10 nM CN and terminated after 30 s, with the exception of measurements for pRIIα and

584   pRIIβ (black lines, *Figure 1*E & F) where 60 s reactions containing 100 nM CN were used.

585

586   **Quantitative immunoblotting of CA1 neuropil extracts**. Hippocampal slices were prepared from 18-day

587   old male Sprague-Dawley rats. Rats were euthanized by cervical dislocation and 350 μm-thick hippocampal

588   slices were collected using a Leica VT1200S microtome in ice-cold sucrose-based saline (189 mM sucrose,

589   10 mM glucose, 3 mM KCl, 5 mM MgSO$_4$, 26 mM NaHCO$_3$, 1.25 mM NaH$_2$PO$_4$, 0.1 mM CaCl$_2$, pH 7.4)

590   saturated with 95% O$_2$/5% CO$_2$. Slices were next transferred to a storage chamber filled with artificial

591   cerebrospinal fluid (aCSF; 124 mM NaCl, 3 mM KCl, 24 mM NaHCO$_3$, 1.25 mM NaH$_2$PO$_4$, 1 mM MgSO$_4$,

592   10 mM glucose, 2 mM CaCl$_2$, pH 7.4) saturated with 95% O$_2$/5% CO$_2$ first for one hour at ~ 31 °C and at

593   room temperature thereafter. For micro-dissection, slices were transferred onto a pre-chilled Sylgard-coated

594   90-mm petri dish atop a dry ice/ethanol bath. The CA1 neuropil layer was micro-dissected using an angled

595   micro-knife (Cajigas et al., 2012) by first cutting along the borders of the stratum pyramidale/stratum

596   radiatum and the stratum lacunosum moleculare/hippocampal fissure. Subsequent lateral cuts at the CA2-

597   CA1 and subiculum-CA1 borders completed the rectangular micro-slices. Micro-dissected neuropil slices

598   were immediately snap frozen in liquid nitrogen and stored at -80 °C. To extract protein, neuropil slices (~

599   15 per animal) were first pulverized with a micro-pestle then resuspended in a final volume of 300 μL

600   extraction buffer (50 mM Tris-HCl, 50 mM NaF, 10 mM EGTA, 10 mM EDTA, 0.08 mM sodium

601   molybdate, 5 mM sodium pyrophosphate, 1 mM penylmethylsulfonyl fluoride, 0.5 % mM Igepal CA-630,

602   0.25% mM sodium deoxycholate, 4 mM para-nitrophenylphosphate, cOmplete EDTA-free protease

23

603   inhibitors and PhosStop phosphatase inhibitors (Roche) at 1 tablet each per 50 mL). The homogenate was

604   sonicated briefly (30 s at 20 MHz) then clarified by centrifugation at 21,130 x g (15 min at 4 °C). Total

605   protein concentration in each extract was determined by BCA assay. Quantitative immunoblotting was

606   performed as described previously (Walker-Gray et al., 2017) using anti-PKA subunit primary antibodies

607   purchased from BD Biosciences. HRP-conjugated secondary antibodies were detected with WesternBright

608   ECL chemiluminescent HRP substrate using a ImageQuant imaging unit (GE Healthcare). Band intensities

609   for reference protein standards and neuropil extracts were calculated in ImageJ. For each immunoblot, a

610   reference curve was generated by fitting reference protein concentrations and band intensities to a Hill

611   function (with typical R^2 coefficients > 0.99) using iterative least squares refinement with the Levenberg-

612   Marquardt algorithm in Origin (OriginLab). PKA subunit concentrations in neuropil extracts were

613   determined by cross-referencing to reference curves derived from the same immunoblot.

614

615   **AKAR4 measurements**. AKAR4 fluorescence measurements were performed using black-walled 96-well

616   plates in a FLUOstar Omega microplate reader (BMG Labtech) equipped with a 430nm excitation filter,

617   and 485nm/520nm emission filters. Each 50 μL reaction contained 35 μL proteins mixed in dilution buffer

618   (20 mM HEPES pH 7.5 and 100 mM NaCl) including AKAR4 reporter (0.2 μM final concentration in all

619   cases) and 5 μL of 10 x reaction buffer (20 mM Na HEPES pH 7.5, 100 mM NaCl, 10 mM DTT, 100 mM

620    $MgCl_2$, 10 mM $CaCl_2$, 0.5 % Igepal CA-630). After three baseline measurements, PKA phosphorylation

621   was initiated by addition of 10 μL solution containing ATP and the desired concentration of cAMP using

622   two injectors built into the plate reader. One injector was primed with ATP solution (20 mM Na HEPES

623   pH 7.5, 100 mM NaCl, 25 mM ATP) and the other with ATP/cAMP solution (20 mM Na HEPES pH 7.5,

624   100 mM NaCl, 25 mM ATP, 2.5 or 10 μM cAMP) so that different proportions of the two injectors could

625   be used to vary the final cAMP concentration. Measurements were collected at 5 second intervals for a

626   minimum of 10 minutes at 22 ºC following injection of ATP. For every run, one control well was included

627   in which AKAR4 was omitted from the protein mixture to enable baseline subtraction. Run parameters

628   were set using Reader Control Software for FLUOstar Omega, and measurements were analyzed using

629   MARS Data Analysis Software (BMG Labtech). Aliquots of a single AKAR4 purification were used across

630   all experiments.

631

632   **Kinetic modeling**. The model scheme of PKA activation is an updated and extended version of the one

633   published by Buxbaum and Dudai (Buxbaum & Dudai, 1989). The model was simulated in a single reaction

634   compartment devoid of any geometry as a system of chemical reactions mimicking the experimental

635   conditions listed above. The individual chemical reactions were modeled as ordinary differential equation

636   (ODE) using the chemical mass-action equation, as:

637

$$A + B \underset{k_r}{\overset{k_f}{\Longleftrightarrow}} AB$$

639
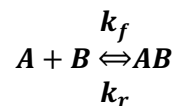
$$-\frac{d[A]}{dt} = -\frac{d[B]}{dt} = \frac{d[AB]}{dt} = k_f(x) = k_f[A][B] = k_r[AB]$$

641

In total, there were 16 chemical species and 16 reactions included in the model, incorporating mostly bi-molecular reactions with forward and backward reaction rates. Enzymatic reactions were represented by the three elementary steps of binding, dissociation and catalysis. All model variants were built using the MATLAB Simbiology toolbox (MathWorks). All reactions, along with initial concentrations of all chemical species and kinetic rates, are listed in *Supplementary Table 1*.

PKA activation follows a sequential binding of four cAMP molecules to the PKA regulatory RII subunit holoenzyme followed by the release (or activation) of two active catalytic subunits (Taylor et al., 2019). However, the chosen modeling approach involved some simplifications: (1) The two RII subunits within the holoenzyme were assumed to behave independently – whereas in reality, some cooperativity is observed in PKA activation due to intra-dimeric contacts within the PKA holoenzymes (Taylor et al., 2012); (2) The two cAMP binding sites on the RII subunit were modelled as a single binding event such that binding of cAMP to RII/pRII is first order with respect to cAMP (Hao et al., 2019). This simplification was incorporated as our focus here was on understanding transitions between pRII and RII subunits and not the precise mechanism of cAMP activation; (3) The respective dephosphorylation parameters for both pRII and pRII bound to cAMP were assumed to be equal; (4) Rates of RII phosphorylation by bound C subunit were assumed to be equal irrespective of whether cAMP was bound to the regulatory subunit; (5) RIIα and RIIβ were assumed to behave similarly since isoform-specific differences were not the focus here. These simplifications were used to reduce the number of model parameters.

Parameters corresponding to the reactions involving dephosphorylation by CN were modified to represent the situations 'with' and 'without' AKAP79 (*Supplementary Table 1*). In total twelve different experimental AKAR4 responses were used to estimate the model parameters. Six corresponded to data shown in *Figure 3*C & E collected with either 1 or 2 μM cAMP activation: conditions with PKA (II) + CaM either alone, with CN, or with both CN and AKAP79. The other six correspond to the calibration curves of C subunit interaction with AKAR4 (*Figure 3-figure supplement* 1A), which were used to estimate AKAR4 parameters that were kept frozen when the other model parameters were estimated. All parameters were estimated using an approximate Bayesian computation (ABC) approach, which included copulas for merging of different experimental data sets (Eriksson et al., 2019). A Bayesian approach was

25

669 used over optimization for a single parameter set, to account for the uncertainty in parameter space, and

670 that more than one set of parameters could fit the data. The result is thus described using distributions for

671 possible parameter values, rather than single values. Initial prior knowledge about the possible parameter

672 ranges using data from this study, and previously published work from other groups (Buxbaum & Dudai,

673 1989; Isensee et al., 2018; Moore et al., 2003; Ogreid & Doskeland, 1981; Stemmer & Klee, 1994; Zhang

674 et al., 2015; Zhang et al., 2012), was used to initiate the parameter fitting (details in ***Supplementary Table***

675 ***1***). This was formalized as using a log uniform prior distribution for the ABC-method. Many of the

676 parameters were set to have a 'prior' range which varied two orders of magnitude from a default parameter

677 value (black bar in ***Figure 5-figure supplement 1***A). For each parameter value, the default parameter value

678 was retrieved from the literature or measurements performed in this study (***Supplementary Table 1***).

679 Simulations were started with initial conditions mimicking the experimental settings, thus for the WT

680 system the initial conditions were assumed to reflect that all RII were either free or bound to C with no

681 phosphorylated species or interactions with cAMP. Simulations were then run for the same length as time

682 as the experiments, assuming the cAMP was added at t=0 and that autophosphorylation started at that time.

683 For predicting responses with mutant RIIα subunits, the base model was extended by splitting the

684 RII into two pools, namely RIIα (85%) and RIIβ (15%) but keeping the parameter distribution received

685 from the parameter estimation when only one isoform of RII was accounted for. Experiments with WT RII

686 subunits were successfully re-simulated with the extended model to validate the approach. As the mutations

687 when simulating both S98A and S98E were in the RIIα subtype (85%), the corresponding parameters

688 depicting the mutation were only varied for this pool. Both the mutant forms, S98A and S98E, were tested

689 as different model variants. To mimic the conditions of the S98A mutation in the model, the

690 phosphorylation rates of RIIα and RIIα bound with cAMP were set to zero (i.e. for the RIIα partition of

691 the model, kinetics were restricted to the right-hand square sub-system shown in ***Figure 4***D). Here the

692 initial conditions were estimated in the same way as described above. To mimic the S98E mutation in the

693 model, the turnover number for dephosphorylation of pRIIα and pRIIα with cAMP by CN were set to zero

694 (i.e. for the RIIα partition of the model, kinetics were restricted to the left-hand square in ***Figure 4***D). Since

695 S98E mimics a case where all the RII subunits are phosphorylated, in this case initial conditions were such

696 that all RIIα were distributed between pRIIα and pRIIα-C.

697 All model variants were built using the MATLAB Simbiology toolbox (MathWorks). Simulations

698 of these reaction systems were performed using the ode15s solver. All simulations were run for 605 s and

699 the AKAR4 phosphorylation was extracted as output to compare with the experimental findings. The model

700 equations were also exported to the statistical programming language R (https://www.r-project.org/) for

701 implementing the parameter estimation through the ABC-copula approach(Eriksson et al., 2019) and only

702 accept parameter sets whose simulated phosphorylated AKAR4 curves reproduced the experimental

703 measurements. A slight modification to the distance measure ρ was, however, introduced to include

704 timeseries data. The sampling was terminated when it had reached approximately 10,000 parameter samples

705 (a subset of which are shown in ***Figure 5-figure supplement 1***A) which all fitted the experimental data

706 within a threshold set to $\rho < 0.01$. All parameter set samples, describing the uncertainty in the parameter

707 estimates, were next projected onto the situations with mutant RIIα subunits. The model immediately

708 reproduced the experimental observations with RIIα S98E subunits. Although the model correctly

709 reproduced lower rates of AKAR4 that occur with RIIα S98A subunits, and that suppression of PKA activity

710 by AKAP79/CN is reduced in this case, there was a substantial spread in the simulated responses in this

711 case. This indicated that WT data had not perfectly constrained the dynamics in the unphosphorylated RII

712 sub-system (right-hand square, ***Figure 4***B). Therefore, to better understand which parameter characteristics

713 that were important to also account for the RIIα S98A, the parameter sets were sub-classified based on how

714 well they fit data collected with RIIα S98A subunits and no CN (light red, ***Figure 5***C) using a threshold of

715 0.03. The parameter sets and its effect on different chemical species of the model were described by multi-

716 trajectory, pairwise coordinate and boxplots, where the color schemes follow the classification described

717 above. A code repository for this study may be accessed at

718 https://drive.google.com/drive/folders/1rNP7jDsLhWpCd8r7vt-eKUCf0eJScHT9.

719

720 **Lentivirus construction**. Lentiviruses were generated by inserting RIIα-IRES2-GFP expression cassettes

721 into a pFUGW-H1 lentiviral vector (Addgene cat no. 25870) containing a shRNA sequence targeting for

722 rat RIIα. In the first step, coding sequence for rat PKA RIIα was isolated from a cDNA library that we

723 generated from total hippocampal RNA from a 7-day old male Sprague Dawley rat bred in the UCL colony.

724 RNA was extracted using an RNeasy Mini Kit before the cDNA library was generated using the first-strand

725 cDNA synthesis kit. Coding sequence for RIIα was amplified from the library using primers Prkar2a_F &

726 Prkar2a_R and inserted upstream of the IRES2 sequence in pIRES2-GFP (Clontech) using EcoRI and

727 BamHI entry sites. Three pFUGW-H1-shRIIα vectors were constructed to determine an optimal targeting

728 sequence for knockdown of rat RIIα. The targeting sequences (primer pairs shRIIα_F1/R1, shRIIα_F2/R2,

729 and shRIIα_F3/R3) were inserted using the XbaI site of pFUGW-H1. The efficiency of each targeting

730 sequence was determined by co-transfecting HEK293T cells with pIRES2-RIIα-EGFP and each pFUGW-

731 H1 vector, with the pFUGW vector in a 10-fold excess. Anti-RIIα immunoblotting revealed that sequence

732 shRIIα-1, which targets bases 134-154 in the rat RIIα coding sequence, was particularly effective at

733 knocking down RIIα protein levels (***Figure 6***B) so this variant served as the parent pFUGW-H1-shRIIα

734 vector in the subsequent steps. The coding sequence for RIIα in pIRES2-RIIα-GFP was rendered shRNA-

735 resistant ('RIIα*') by SDM with primers Prkar2a_shRNA_resist_F & R. After introducing an NheI entry

736 site into pFUGW-H1-shRIIα by SDM using primers FUGW_NheI_F & R, the dual expression cassette for

737 RIIα-IRES2-GFP was transferred across into pFUGW-H1-shRIIα downstream of the ubiquitin promoter

738 using NheI and AgeI sites to create the complete lentiviral vector pFUGW-H1-shRIIα-RIIα*-IRES2-EGFP.

739 Vectors containing RIIα replacement sequences with mutations at S97 were obtained by SDM with

740 primers pairs rS97A_F & R and rS97E_F & R. In addition, a control vector containing a scrambled shRNA

741 sequence was constructed using primers shScram_F & R. To produce lentivirus, pFUGW vectors were co-

742 transfected with pCMVdR8.74 packaging vector (Addgene cat no. 12259) and pMD2.G envelope

743 glycoprotein vector (Addgene cat no. 12259) into HEK293 cells using Lipofectamine 2000 and maintained

744 in DMEM supplemented with 10% FBS. Cell culture media was collected at both 48 and 72 hours after

745 transfection, subjected to 0.45 μm filtering, and centrifuged at 48,384 x g for 4 hours at 4°C to concentrate

746 viral particles. Pelleted virus was resuspended in sterile PBS and stored at – 80 °C. Lentiviruses were

747 validated by transducing dissociated hippocampal cultures on DIV7. Neurons were collected on DIV14,

748 and protein extracted using sonication (3 x 10 s at 20 MHz) in extraction buffer. The homogenate was

749 clarified by centrifugation at 21,130 x g for 15 minutes before analysis of protein levels in the supernatant

750 by immunoblotting using antibodies including anti-PKA pRIIα (Abcam, RRID: AB_779040), anti-GFP

751 (Sigma Aldrich, RRID: AB_2750576), and anti-β-tubulin antibodies (Biolegend, RRID: AB_2565030).

752

753 **Lentiviral infection and imaging of dissociated primary hippocampal neurons**. Primary hippocampal

754 cultures were cultured from E18 Sprague-Dawley pups. Hippocampi were isolated and triturated with

755 trypsin (0.025%) before plating on poly-L-lysine-coated coverslips or 6-well plates in DMEM containing

756 10% heat-inactivated horse serum, and penicillin (40 U/mL)/streptomycin (40 μg/mL). Neurons were

757 cultured at 37°C in 95% air/5% CO_2. Two hours after seeding, the plating media was replaced with

758 Neurobasal-A supplemented with 1% B27, 0.5% (v/v) GlutaMAX, 20 mM glucose, and penicillin (100

759 U/mL)/streptomycin (100 μg/mL). Culture media and additives were purchased from Gibco with the

760 exception of GlutaMAX (Thermo Fisher Scientific). Neurons were infected with lentivirus at DIV7 or DIV9

761 for dendritic spine density and time-lapse experiments, respectively. Concentrated viral stocks were diluted

762 in conditioned media and incubated with neurons for 18 hours before replacing with fresh pre-conditioned

763 media. Live-cell confocal imaging of dendritic spines was performed using an upright Zeiss LSM 510

764 confocal microscope equipped with an Achroplan 40x water differential interference contrast objective

765 (numerical aperture 0.8). Transduced neurons were washed four times in HEPES-buffered Krebs solution

766 (140 mM NaCl, 4.2 mM KCl, 1.2 mM $MgCl_2$, 2.52 mM $CaCl_2$, 5 mM Na HEPES, and 11 mM glucose,

767 adjusted to pH 7.4 with NaOH) and placed into a chamber in this same solution at room temperature. For

768 each dendritic segment, upper and lower bounds in the z-plane were initially determined using a rapid z-

769 scan. A full image stack was then collected using a 488 nm Argon laser and a 505-530 nm band-pass

770 emission filter for imaging EGFP fluorescence using 512 x 512 frames with 3-line averaging, and optical

771 slice spacing of 1.035 μm. Time-lapse experiments were conducted to measure changes in spine density

772 and spine-head size after the induction of chemical LTD. An optical slice spacing of 0.9 μm was used

773 during time-lapse experiments. Z-stacks were acquired every 5 min from 15 min before to 60 min after the

774 induction of chemical LTD. Bath application of 20 μM NMDA for 3 min was used to induce NMDAR-

775 dependent LTD (Lee et al., 1998). Data was deconvolved using ImageJ (NIH) before automated dendrite

776 identification and classification in NeuronStudio (Rodriguez et al., 2008). In time-lapse experiments,

777 dendritic spine densities were normalized to the value at t=0.

778

779 **Statistical analysis**. All data are presented as means ± SE. Kinetic rates were statistically compared using

780 two-tailed unpaired Student *t*-tests. Spine imaging data was compared by ANOVA with Turkey post-hoc

781 tests (***Figure 6***D) and Bonferroni's post-hoc test (***Figure 6***G). *$p < 0.05$; **$p < 0.01$; ***$p < 0.001$.

782

783

Author Contributions

785 T.C. performed CA1 neuropil dissections, quantitative immunoblots, developed the lentiviral targeting

786 vectors, and imaged structural plasticity in dendrites. P.T. J.A, O.E and J.H.K. built and simulated the

787 AKAP79-PKA-CN signaling model. S.H. imaged and analyzed spine numbers in primary hippocampal

788 neurons with support from T.G.S. M.G.G. conceived the study, purified proteins, and performed and

789 analyzed phosphatase assays and AKAR4 recordings. M.G.G. and T.C. wrote the manuscript with input

790 from all the authors.

791

Acknowledgements

802

References

Aye, T. T., Scholten, A., Taouatas, N., Varro, A., Van Veen, T. A., Vos, M. A., & Heck, A. J. (2010, Oct). Proteome-wide protein concentrations in the human heart. *Mol Biosyst, 6*(10), 1917-1927. https://doi.org/10.1039/c004495d

Baillie, G. S., Tejeda, G. S., & Kelly, M. P. (2019, Oct). Therapeutic targeting of 3',5'-cyclic nucleotide phosphodiesterases: inhibition and beyond. *Nat Rev Drug Discov, 18*(10), 770-796. https://doi.org/10.1038/s41573-019-0033-4

Baldwin, T. A., & Dessauer, C. W. (2018, Jan 16). Function of Adenylyl Cyclase in Heart: the AKAP Connection. *J Cardiovasc Dev Dis, 5*(1). https://doi.org/10.3390/jcdd5010002

Bear, M. F. (2003, Apr 29). Bidirectional synaptic plasticity: from theory to reality. *Philos Trans R Soc Lond B Biol Sci, 358*(1432), 649-655. https://doi.org/10.1098/rstb.2002.1255

Bers, D. M., Xiang, Y. K., & Zaccolo, M. (2019, Jul 1). Whole-Cell cAMP and PKA Activity are Epiphenomena, Nanodomain Signaling Matters. *Physiology (Bethesda), 34*(4), 240-249. https://doi.org/10.1152/physiol.00002.2019

Bock, A., Annibale, P., Konrad, C., Hannawacker, A., Anton, S. E., Maiellaro, I., Zabel, U., Sivaramakrishnan, S., Falcke, M., & Lohse, M. J. (2020, Sep 17). Optical Mapping of cAMP Signaling at the Nanometer Scale. *Cell, 182*(6), 1519-1530 e1517. https://doi.org/10.1016/j.cell.2020.07.035

Buxbaum, J. D., & Dudai, Y. (1989, Jun 5). A quantitative model for the kinetics of cAMP-dependent protein kinase (type II) activity. Long-term activation of the kinase and its possible relevance to learning and memory. *J Biol Chem, 264*(16), 9344-9351. https://www.ncbi.nlm.nih.gov/pubmed/2722837

Cajigas, I. J., Tushev, G., Will, T. J., tom Dieck, S., Fuerst, N., & Schuman, E. M. (2012, May 10). The local transcriptome in the synaptic neuropil revealed by deep sequencing and high-resolution imaging. *Neuron, 74*(3), 453-466. https://doi.org/10.1016/j.neuron.2012.02.036

Clouet, D. H., & Gaitonde, M. K. (1956, Dec). The changes with age in the protein composition of the rat brain. *J Neurochem, 1*(2), 126-133. https://doi.org/10.1111/j.1471-4159.1956.tb12063.x

Coghlan, V. M., Perrino, B. A., Howard, M., Langeberg, L. K., Hicks, J. B., Gallatin, W. M., & Scott, J. D. (1995, Jan 6). Association of protein kinase A and protein phosphatase 2B with a common anchoring protein. *Science, 267*(5194), 108-111.

843   http://www.ncbi.nlm.nih.gov/entrez/query.fcgi?cmd=Retrieve&db=PubMed&dopt=Citation&list
844   _uids=7528941
845

846   Dacher, M., Gouty, S., Dash, S., Cox, B. M., & Nugent, F. S. (2013, Feb 6). A-kinase anchoring protein-
847   calcineurin signaling in long-term depression of GABAergic synapses. *J Neurosci, 33*(6), 2650-
848   2660. https://doi.org/10.1523/JNEUROSCI.2037-12.2013
849

850   Delint-Ramirez, I., Willoughby, D., Hammond, G. R., Ayling, L. J., & Cooper, D. M. (2011, Sep 23).
851   Palmitoylation targets AKAP79 protein to lipid rafts and promotes its regulation of calcium-
852   sensitive adenylyl cyclase type 8. *J Biol Chem, 286*(38), 32962-32975.
853   https://doi.org/10.1074/jbc.M111.243899
854

855   Dell'Acqua, M. L., Dodge, K. L., Tavalin, S. J., & Scott, J. D. (2002, Dec 13). Mapping the protein
856   phosphatase-2B anchoring site on AKAP79. Binding and inhibition of phosphatase activity are
857   mediated by residues 315-360. *J Biol Chem, 277*(50), 48796-48802.
858   https://doi.org/10.1074/jbc.M207833200
859

860   Dell'Acqua, M. L., Faux, M. C., Thorburn, J., Thorburn, A., & Scott, J. D. (1998, Apr 15). Membrane-
861   targeting sequences on AKAP79 bind phosphatidylinositol-4, 5-bisphosphate. *Embo J, 17*(8),
862   2246-2260.
863   http://www.ncbi.nlm.nih.gov/entrez/query.fcgi?cmd=Retrieve&db=PubMed&dopt=Citation&list
864   _uids=9545238
865

866   Depry, C., Allen, M. D., & Zhang, J. (2011, Jan). Visualization of PKA activity in plasma membrane
867   microdomains [Research Support, N.I.H., Extramural]. *Mol Biosyst, 7*(1), 52-58.
868   https://doi.org/10.1039/c0mb00079e
869

870   Dittmer, P. J., Dell'Acqua, M. L., & Sather, W. A. (2014, Jun 12). Ca2+/calcineurin-dependent
871   inactivation of neuronal L-type Ca2+ channels requires priming by AKAP-anchored protein
872   kinase A. *Cell Rep, 7*(5), 1410-1416. https://doi.org/10.1016/j.celrep.2014.04.039
873

874   Eriksson, O., Jauhiainen, A., Maad Sasane, S., Kramer, A., Nair, A. G., Sartorius, C., & Hellgren
875   Kotaleski, J. (2019, Jan 15). Uncertainty quantification, propagation and characterization by
876   Bayesian analysis combined with global sensitivity analysis applied to dynamical intracellular
877   pathway models. *Bioinformatics, 35*(2), 284-292. https://doi.org/10.1093/bioinformatics/bty607
878

879   Gold, M. G. (2019, Oct 31). Swimming regulations for protein kinase A catalytic subunit. *Biochem Soc
880   Trans, 47*(5), 1355-1366. https://doi.org/10.1042/BST20190230
881

882   Gold, M. G., Lygren, B., Dokurno, P., Hoshi, N., McConnachie, G., Tasken, K., Carlson, C. R., Scott, J.
883   D., & Barford, D. (2006). Molecular basis of AKAP specificity for PKA regulatory subunits.
884   *Molecular cell, 24*(3), 383-395. <Go to ISI>://MEDLINE:17081989

31

885

886   Gold, M. G., Stengel, F., Nygren, P. J., Weisbrod, C. R., Bruce, J. E., Robinson, C. V., Barford, D., &
887   Scott, J. D. (2011, Apr 19). Architecture and dynamics of an A-kinase anchoring protein 79
888   (AKAP79) signaling complex. *Proc Natl Acad Sci U S A, 108*(16), 6426-6431.
889   https://doi.org/1014400108 [pii]
890   10.1073/pnas.1014400108
891

892   Hinke, S. A., Navedo, M. F., Ulman, A., Whiting, J. L., Nygren, P. J., Tian, G., Jimenez-Caliani, A. J.,
893   Langeberg, L. K., Cirulli, V., Tengholm, A., Dell'Acqua, M. L., Santana, L. F., & Scott, J. D.
894   (2012, Oct 17). Anchored phosphatases modulate glucose homeostasis. *Embo J, 31*(20), 3991-
895   4004. https://doi.org/10.1038/emboj.2012.244
896

897   Hogan, P. G. (2017, May). Calcium-NFAT transcriptional signalling in T cell activation and T cell
898   exhaustion. *Cell Calcium, 63*, 66-69. https://doi.org/10.1016/j.ceca.2017.01.014
899

900   Hoshi, N., Langeberg, L. K., Gould, C. M., Newton, A. C., & Scott, J. D. (2010, Feb 26). Interaction with
901   AKAP79 modifies the cellular pharmacology of PKC. *Molecular cell, 37*(4), 541-550.
902   https://doi.org/10.1016/j.molcel.2010.01.014
903

904   Houslay, M. D., & Baillie, G. S. (2005, Dec). Beta-arrestin-recruited phosphodiesterase-4 desensitizes the
905   AKAP79/PKA-mediated switching of beta2-adrenoceptor signalling to activation of ERK.
906   *Biochem Soc Trans, 33*(Pt 6), 1333-1336. https://doi.org/10.1042/BST20051333
907

908   Huang, Y. Y., Li, X. C., & Kandel, E. R. (1994, Oct 7). cAMP contributes to mossy fiber LTP by
909   initiating both a covalently mediated early phase and macromolecular synthesis-dependent late
910   phase. *Cell, 79*(1), 69-79. https://doi.org/10.1016/0092-8674(94)90401-4
911

912   Ilouz, R., Lev-Ram, V., Bushong, E. A., Stiles, T. L., Friedmann-Morvinski, D., Douglas, C., Goldberg,
913   G., Ellisman, M. H., & Taylor, S. S. (2017, Jan 12). Isoform-specific subcellular localization and
914   function of protein kinase A identified by mosaic imaging of mouse brain. *Elife, 6*.
915   https://doi.org/10.7554/eLife.17681
916

917   Isensee, J., Kaufholz, M., Knape, M. J., Hasenauer, J., Hammerich, H., Gonczarowska-Jorge, H., Zahedi,
918   R. P., Schwede, F., Herberg, F. W., & Hucho, T. (2018, Jun 4). PKA-RII subunit phosphorylation
919   precedes activation by cAMP and regulates activity termination. *J Cell Biol, 217*(6), 2167-2184.
920   https://doi.org/10.1083/jcb.201708053
921

922   Jurado, S., Biou, V., & Malenka, R. C. (2010, Sep). A calcineurin/AKAP complex is required for NMDA
923   receptor-dependent long-term depression. *Nat Neurosci, 13*(9), 1053-1055.
924   https://doi.org/nn.2613 [pii]
925   10.1038/nn.2613
926

927   Kar, P., Samanta, K., Kramer, H., Morris, O., Bakowski, D., & Parekh, A. B. (2014, Jun 16). Dynamic
928   assembly of a membrane signaling complex enables selective activation of NFAT by Orai1. *Curr*
929   *Biol, 24*(12), 1361-1368. https://doi.org/10.1016/j.cub.2014.04.046
930

931   Kashishian, A., Howard, M., Loh, C., Gallatin, W. M., Hoekstra, M. F., & Lai, Y. (1998, Oct 16).
932   AKAP79 inhibits calcineurin through a site distinct from the immunophilin-binding region. *J Biol*
933   *Chem, 273*(42), 27412-27419. https://doi.org/10.1074/jbc.273.42.27412
934

935   Keith, D. J., Sanderson, J. L., Gibson, E. S., Woolfrey, K. M., Robertson, H. R., Olszewski, K., Kang, R.,
936   El-Husseini, A., & Dell'acqua, M. L. (2012, May 23). Palmitoylation of A-kinase anchoring
937   protein 79/150 regulates dendritic endosomal targeting and synaptic plasticity mechanisms. *J*
938   *Neurosci, 32*(21), 7119-7136. https://doi.org/10.1523/JNEUROSCI.0784-12.2012
939

940   Kinderman, F. S., Kim, C., von Daake, S., Ma, Y., Pham, B. Q., Spraggon, G., Xuong, N.-H., Jennings, P.
941   A., & Taylor, S. S. (2006). A dynamic mechanism for AKAP binding to RII isoforms of cAMP-
942   dependent protein kinase. *Molecular cell, 24*(3), 397-408. <Go to ISI>://MEDLINE:17081990
943

944   Kwon, H. B., & Sabatini, B. L. (2011, Jun 2). Glutamate induces de novo growth of functional spines in
945   developing cortex. *Nature, 474*(7349), 100-104. https://doi.org/10.1038/nature09986
946

947   Lee, H. K., Kameyama, K., Huganir, R. L., & Bear, M. F. (1998, Nov). NMDA induces long-term
948   synaptic depression and dephosphorylation of the GluR1 subunit of AMPA receptors in
949   hippocampus. *Neuron, 21*(5), 1151-1162. https://doi.org/10.1016/s0896-6273(00)80632-7
950

951   Li, H., Pink, M. D., Murphy, J. G., Stein, A., Dell'Acqua, M. L., & Hogan, P. G. (2012, Feb 19). Balanced
952   interactions of calcineurin with AKAP79 regulate Ca2+-calcineurin-NFAT signaling. *Nat Struct*
953   *Mol Biol, 19*(3), 337-345. https://doi.org/10.1038/nsmb.2238
954

955   Lu, Y., Zha, X. M., Kim, E. Y., Schachtele, S., Dailey, M. E., Hall, D. D., Strack, S., Green, S. H.,
956   Hoffman, D. A., & Hell, J. W. (2011, Jul 29). A kinase anchor protein 150 (AKAP150)-
957   associated protein kinase A limits dendritic spine density. *J Biol Chem, 286*(30), 26496-26506.
958   https://doi.org/10.1074/jbc.M111.254912
959

960   Lu, Y., Zhang, M., Lim, I. A., Hall, D. D., Allen, M., Medvedeva, Y., McKnight, G. S., Usachev, Y. M.,
961   & Hell, J. W. (2008, Sep 1). AKAP150-anchored PKA activity is important for LTD during its
962   induction phase. *J Physiol, 586*(17), 4155-4164. https://doi.org/10.1113/jphysiol.2008.151662
963

964   Moore, M. J., Adams, J. A., & Taylor, S. S. (2003, Mar 21). Structural basis for peptide binding in protein
965   kinase A. Role of glutamic acid 203 and tyrosine 204 in the peptide-positioning loop. *J Biol*
966   *Chem, 278*(12), 10613-10618. https://doi.org/10.1074/jbc.M210807200
967

968 Mulkey, R. M., Endo, S., Shenolikar, S., & Malenka, R. C. (1994, Jun 9). Involvement of a
969   calcineurin/inhibitor-1 phosphatase cascade in hippocampal long-term depression. *Nature,*
970   *369*(6480), 486-488. https://doi.org/10.1038/369486a0
971

972 Murphy, J. G., Sanderson, J. L., Gorski, J. A., Scott, J. D., Catterall, W. A., Sather, W. A., & Dell'Acqua,
973   M. L. (2014, Jun 12). AKAP-anchored PKA maintains neuronal L-type calcium channel activity
974   and NFAT transcriptional signaling. *Cell Rep, 7*(5), 1577-1588.
975   https://doi.org/10.1016/j.celrep.2014.04.027
976

977 Ni, Q., Ganesan, A., Aye-Han, N. N., Gao, X., Allen, M. D., Levchenko, A., & Zhang, J. (2011, Jan).
978   Signaling diversity of PKA achieved via a Ca2+-cAMP-PKA oscillatory circuit. *Nat Chem Biol,*
979   *7*(1), 34-40. https://doi.org/10.1038/nchembio.478
980

981 Nygren, P. J., Mehta, S., Schweppe, D. K., Langeberg, L. K., Whiting, J. L., Weisbrod, C. R., Bruce, J.
982   E., Zhang, J., Veesler, D., & Scott, J. D. (2017, Oct 2). Intrinsic disorder within AKAP79 fine-
983   tunes anchored phosphatase activity toward substrates and drug sensitivity. *Elife, 6.*
984   https://doi.org/10.7554/eLife.30872
985

986 Ogreid, D., & Doskeland, S. O. (1981, Jul 6). The kinetics of the interaction between cyclic AMP and the
987   regulatory moiety of protein kinase II. Evidence for interaction between the binding sites for
988   cyclic AMP. *FEBS Lett, 129*(2), 282-286. https://www.ncbi.nlm.nih.gov/pubmed/6269881
989

990 Patel, N., Stengel, F., Aebersold, R., & Gold, M. G. (2017, Nov 22). Molecular basis of AKAP79
991   regulation by calmodulin. *Nat Commun, 8*(1), 1681. https://doi.org/10.1038/s41467-017-01715-w
992

993 Perrino, B. A., Fong, Y. L., Brickey, D. A., Saitoh, Y., Ushio, Y., Fukunaga, K., Miyamoto, E., &
994   Soderling, T. R. (1992, Aug 5). Characterization of the phosphatase activity of a baculovirus-
995   expressed calcineurin A isoform. *J Biol Chem, 267*(22), 15965-15969.
996   https://www.ncbi.nlm.nih.gov/pubmed/1322410
997

998 Qi, C., Sorrentino, S., Medalia, O., & Korkhov, V. M. (2019, Apr 26). The structure of a membrane
999   adenylyl cyclase bound to an activated stimulatory G protein. *Science, 364*(6438), 389-394.
1000   https://doi.org/10.1126/science.aav0778
1001

1002 Qian, H., Patriarchi, T., Price, J. L., Matt, L., Lee, B., Nieves-Cintron, M., Buonarati, O. R., Chowdhury,
1003   D., Nanou, E., Nystoriak, M. A., Catterall, W. A., Poomvanicha, M., Hofmann, F., Navedo, M.
1004   F., & Hell, J. W. (2017, Jan 24). Phosphorylation of Ser1928 mediates the enhanced activity of
1005   the L-type Ca2+ channel Cav1.2 by the beta2-adrenergic receptor in neurons. *Sci Signal, 10*(463).
1006   https://doi.org/10.1126/scisignal.aaf9659
1007

1008 Rangel-Aldao, R., & Rosen, O. M. (1976, Jun 10). Dissociation and reassociation of the phosphorylated
1009   and nonphosphorylated forms of adenosine 3':5' -monophosphate-dependent protein kinase from

bovine cardiac muscle. *J Biol Chem, 251*(11), 3375-3380.
https://www.ncbi.nlm.nih.gov/pubmed/179996

Redden, J. M., & Dodge-Kafka, K. L. (2011, Oct). AKAP phosphatase complexes in the heart. *J Cardiovasc Pharmacol, 58*(4), 354-362. https://doi.org/10.1097/FJC.0b013e31821e5649

Roach, P. J., Depaoli-Roach, A. A., Hurley, T. D., & Tagliabracci, V. S. (2012, Feb 1). Glycogen and its metabolism: some new developments and old themes. *Biochem J, 441*(3), 763-787. https://doi.org/10.1042/BJ20111416

Rodriguez, A., Ehlenberger, D. B., Dickstein, D. L., Hof, P. R., & Wearne, S. L. (2008, Apr 23). Automated three-dimensional detection and shape classification of dendritic spines from fluorescence microscopy images. *PLoS One, 3*(4), e1997. https://doi.org/10.1371/journal.pone.0001997

Roy, J., & Cyert, M. S. (2009, Dec 8). Cracking the phosphatase code: docking interactions determine substrate specificity. *Sci Signal, 2*(100), re9. https://doi.org/10.1126/scisignal.2100re9

Sanderson, J. L., Gorski, J. A., & Dell'Acqua, M. L. (2016, Mar 2). NMDA Receptor-Dependent LTD Requires Transient Synaptic Incorporation of Ca(2)(+)-Permeable AMPARs Mediated by AKAP150-Anchored PKA and Calcineurin. *Neuron, 89*(5), 1000-1015. https://doi.org/10.1016/j.neuron.2016.01.043

Sanderson, J. L., Gorski, J. A., Gibson, E. S., Lam, P., Freund, R. K., Chick, W. S., & Dell'Acqua, M. L. (2012, Oct 24). AKAP150-anchored calcineurin regulates synaptic plasticity by limiting synaptic incorporation of Ca2+-permeable AMPA receptors. *J Neurosci, 32*(43), 15036-15052. https://doi.org/10.1523/JNEUROSCI.3326-12.2012

Schmitt, J. P., Kamisago, M., Asahi, M., Li, G. H., Ahmad, F., Mende, U., Kranias, E. G., MacLennan, D. H., Seidman, J. G., & Seidman, C. E. (2003, Feb 28). Dilated cardiomyopathy and heart failure caused by a mutation in phospholamban. *Science, 299*(5611), 1410-1413. https://doi.org/10.1126/science.1081578

Stemmer, P. M., & Klee, C. B. (1994, Jun 7). Dual calcium ion regulation of calcineurin by calmodulin and calcineurin B. *Biochemistry, 33*(22), 6859-6866. https://doi.org/10.1021/bi00188a015

Taylor, S. S., Meharena, H. S., & Kornev, A. P. (2019, Jun). Evolution of a dynamic molecular switch. *IUBMB Life, 71*(6), 672-684. https://doi.org/10.1002/iub.2059

1049 Tunquist, B. J., Hoshi, N., Guire, E. S., Zhang, F., Mullendorff, K., Langeberg, L. K., Raber, J., & Scott,
1050   J. D. (2008, Aug 26). Loss of AKAP150 perturbs distinct neuronal processes in mice. *Proc Natl*
1051   *Acad Sci U S A, 105*(34), 12557-12562. https://doi.org/0805922105 [pii]
1052 10.1073/pnas.0805922105
1053

1054 Walker-Gray, R., Stengel, F., & Gold, M. G. (2017, Sep 26). Mechanisms for restraining cAMP-
1055   dependent protein kinase revealed by subunit quantitation and cross-linking approaches. *Proc*
1056   *Natl Acad Sci U S A, 114*(39), 10414-10419. https://doi.org/10.1073/pnas.1701782114
1057

1058 Weisenhaus, M., Allen, M. L., Yang, L., Lu, Y., Nichols, C. B., Su, T., Hell, J. W., & McKnight, G. S.
1059   (2010, Apr 23). Mutations in AKAP5 disrupt dendritic signaling complexes and lead to
1060   electrophysiological and behavioral phenotypes in mice. *PLoS One, 5*(4), e10325.
1061   https://doi.org/10.1371/journal.pone.0010325
1062

1063 Wild, A. R., Sinnen, B. L., Dittmer, P. J., Kennedy, M. J., Sather, W. A., & Dell'Acqua, M. L. (2019, Mar
1064   26). Synapse-to-Nucleus Communication through NFAT Is Mediated by L-type Ca(2+) Channel
1065   Ca(2+) Spike Propagation to the Soma. *Cell Rep, 26*(13), 3537-3550 e3534.
1066   https://doi.org/10.1016/j.celrep.2019.03.005
1067

1068 Woolfrey, K. M., O'Leary, H., Goodell, D. J., Robertson, H. R., Horne, E. A., Coultrap, S. J., Dell'Acqua,
1069   M. L., & Bayer, K. U. (2018, Feb 2). CaMKII regulates the depalmitoylation and synaptic
1070   removal of the scaffold protein AKAP79/150 to mediate structural long-term depression. *J Biol*
1071   *Chem, 293*(5), 1551-1567. https://doi.org/10.1074/jbc.M117.813808
1072

1073 Zhang, J., & Shapiro, M. S. (2012, Dec 20). Activity-dependent transcriptional regulation of M-Type
1074   (Kv7) K(+) channels by AKAP79/150-mediated NFAT actions. *Neuron, 76*(6), 1133-1146.
1075   https://doi.org/10.1016/j.neuron.2012.10.019
1076

1077 Zhang, J., & Shapiro, M. S. (2016, Jan 1). Mechanisms and dynamics of AKAP79/150-orchestrated
1078   multi-protein signalling complexes in brain and peripheral nerve. *J Physiol, 594*(1), 31-37.
1079   https://doi.org/10.1113/jphysiol.2014.287698
1080

1081 Zhang, J. Z., Lu, T. W., Stolerman, L. M., Tenner, B., Yang, J. R., Zhang, J. F., Falcke, M., Rangamani,
1082   P., Taylor, S. S., Mehta, S., & Zhang, J. (2020, Sep 17). Phase Separation of a PKA Regulatory
1083   Subunit Controls cAMP Compartmentation and Oncogenic Signaling. *Cell, 182*(6), 1531-1544
1084   e1515. https://doi.org/10.1016/j.cell.2020.07.043
1085

1086 Zhang, P., Knape, M. J., Ahuja, L. G., Keshwani, M. M., King, C. C., Sastri, M., Herberg, F. W., &
1087   Taylor, S. S. (2015). Single Turnover Autophosphorylation Cycle of the PKA RIIbeta
1088   Holoenzyme. *PLoS biology, 13*(7), e1002192. <Go to ISI>://MEDLINE:26158466
1089

1090 Zhang, P., Smith-Nguyen, E. V., Keshwani, M. M., Deal, M. S., Kornev, A. P., & Taylor, S. S. (2012,
1091   Feb 10). Structure and allostery of the PKA RIIbeta tetrameric holoenzyme. *Science, 335*(6069),
1092   712-716. https://doi.org/10.1126/science.1213979
1093

1094 Zhang, X., Li, L., & McNaughton, P. A. (2008, Aug 14). Proinflammatory mediators modulate the heat-
1095   activated ion channel TRPV1 via the scaffolding protein AKAP79/150. *Neuron, 59*(3), 450-461.
1096   https://doi.org/10.1016/j.neuron.2008.05.015
1097

1098 Zhang, X., Pathak, T., Yoast, R., Emrich, S., Xin, P., Nwokonko, R. M., Johnson, M., Wu, S., Delierneux,
1099   C., Gueguinou, M., Hempel, N., Putney, J. W., Jr., Gill, D. L., & Trebak, M. (2019, Apr 29). A
1100   calcium/cAMP signaling loop at the ORAI1 mouth drives channel inactivation to shape NFAT
1101   induction. *Nat Commun, 10*(1), 1971. https://doi.org/10.1038/s41467-019-09593-0
1102

1103 Zhou, Q., Homma, K. J., & Poo, M. M. (2004, Dec 2). Shrinkage of dendritic spines associated with long-
1104   term depression of hippocampal synapses. *Neuron, 44*(5), 749-757.
1105   https://doi.org/10.1016/j.neuron.2004.11.011
1106

1107

1108

1109   **Supplementary Information**

1110

1111   **Figure 1-figure supplement 1**. Purified proteins.

1112

1113   **Figure 1-figure supplement 2**. pRII phosphorylation by CN at supra-physiological concentrations

1114

1115   **Figure 2-figure supplement 1**. Reference curves for quantitation of PKA subunits in CA1 neuropil

1116

1117   **Figure 3-figure supplement 1**. AKAR4 reference measurements with PKA catalytic subunit

1118

1119   **Figure 4-figure supplement 1**. Simulations of kinetic scheme species changes in concentration over time

1120

1121   **Figure 5-figure supplement 1**. Space of parameters used in model fitting
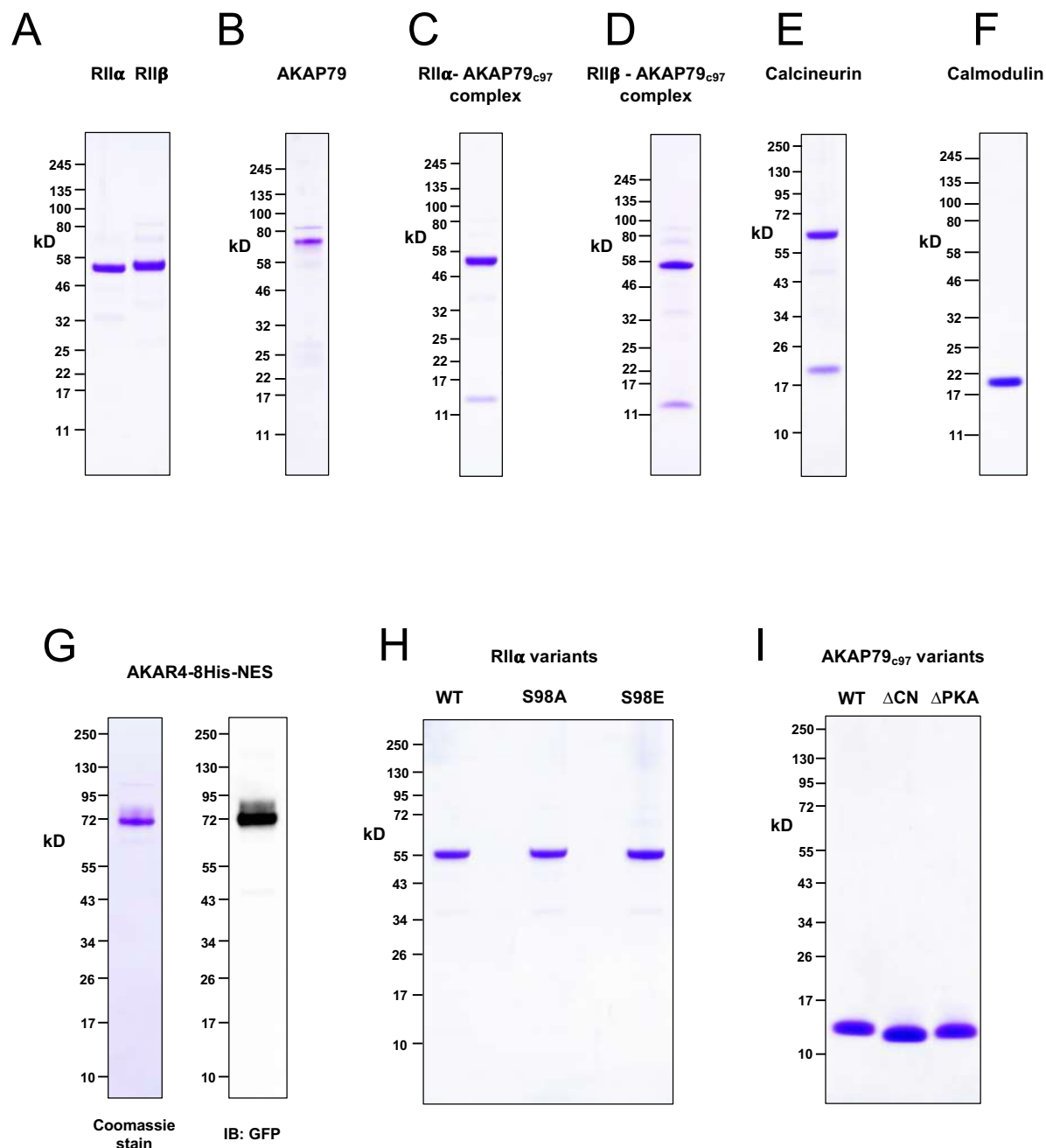
1122

1123   **Supplementary Table 1**. Kinetic modeling parameters

1124

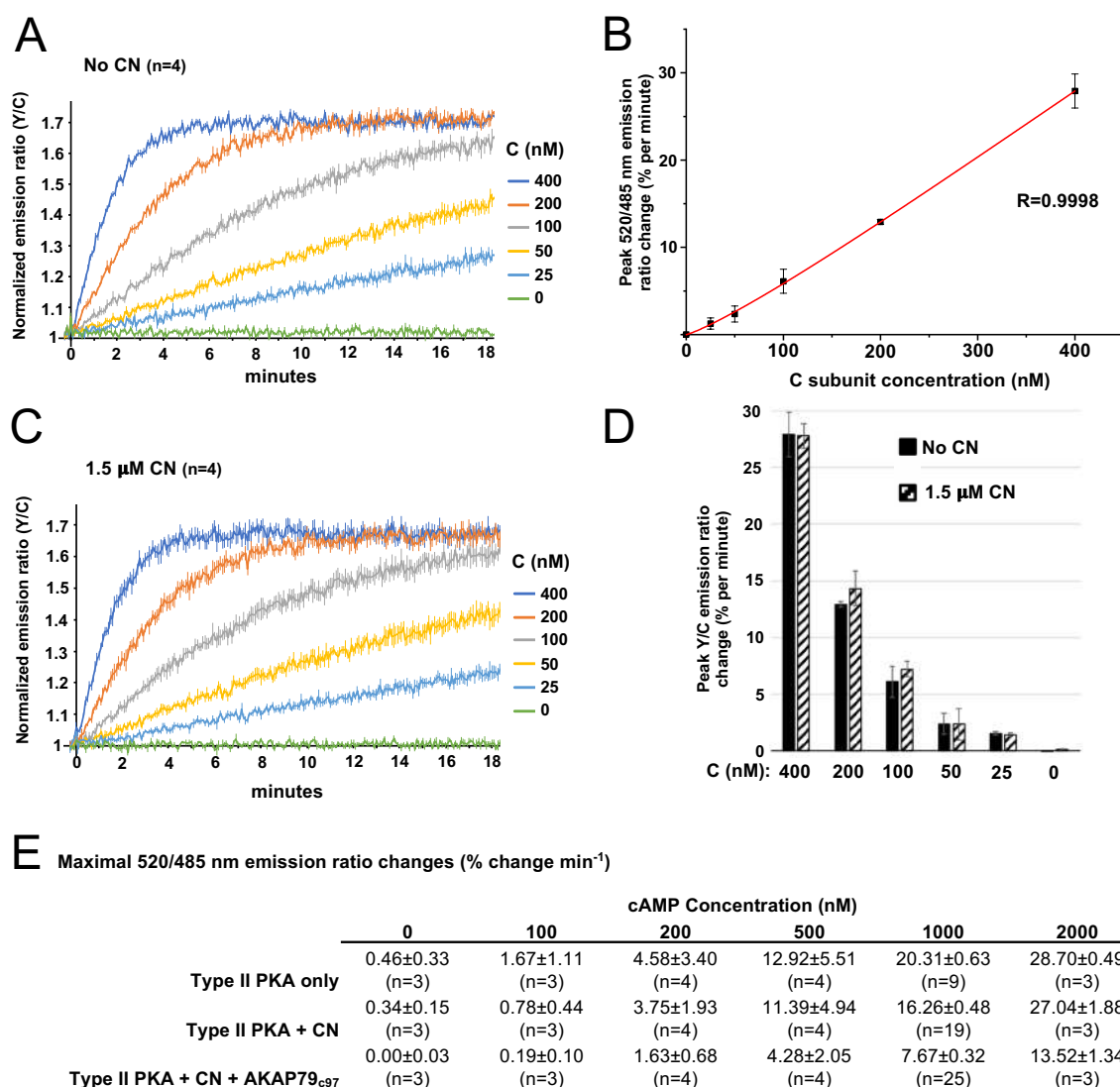1125   **Supplementary Table 2**. Oligonucleotide primer sequences

1126

1127

1128 **Figure 1-figure supplement 1. Purified proteins**. Images showing the purity of purified proteins applied in
1129 this study are shown following SDS-PAGE with 4–12% Bis-Tris NuPAGE gels. (**A**) Full-length WT PKA
1130 RIIα and RIIβ subunits. (**B**) Full-length AKAP79. (**C**) The complex of RIIα and AKAP79$_{c97}$. (**D**) The complex
1131 of RIIβ and AKAP79$_{c97}$. (**E**) The CN heterodimer. (**F**) CaM. (**G**) AKAR4 – the left-hand image shows
1132 Coomassie staining whereas the right-hand image shows anti-GFP immunoblotting of an equivalent lane after
1133 transfer to nitrocellulose. (**H**) Variants of RIIα (WT, S98A, S98E) applied in AKAR4 assays. (**I**) Variants of
1134 AKAP79$_{c97}$ (WT, ΔCN, ΔPKA) applied in AKAR4 assays. All images were scanned following Coomassie
1135 staining unless otherwise stated.
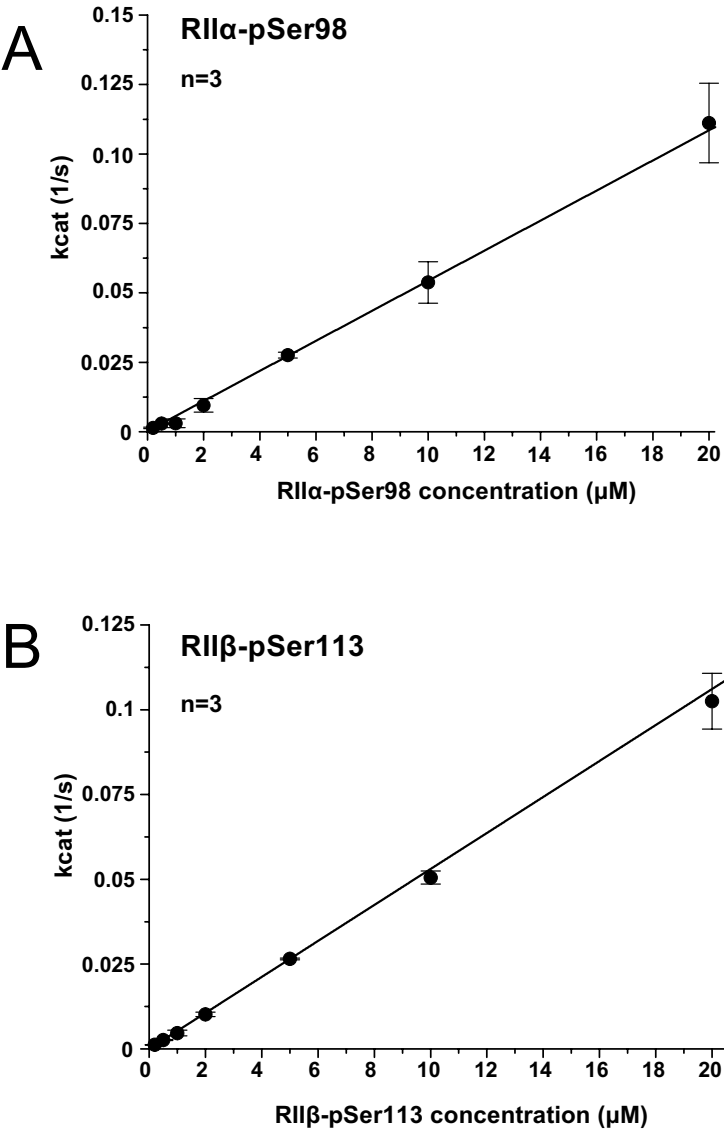
1136

1137

1138

1139 **Figure 1-figure supplement 2. pRII phosphorylation by CN at supra-physiological concentrations**. The
1140 relationship between CN activity towards pRII and pRII concentration in the absence of AKAP79 is linear for
1141 both pRIIα (**A**) and pRIIβ (**B**) up to at least 20 μM pRII.
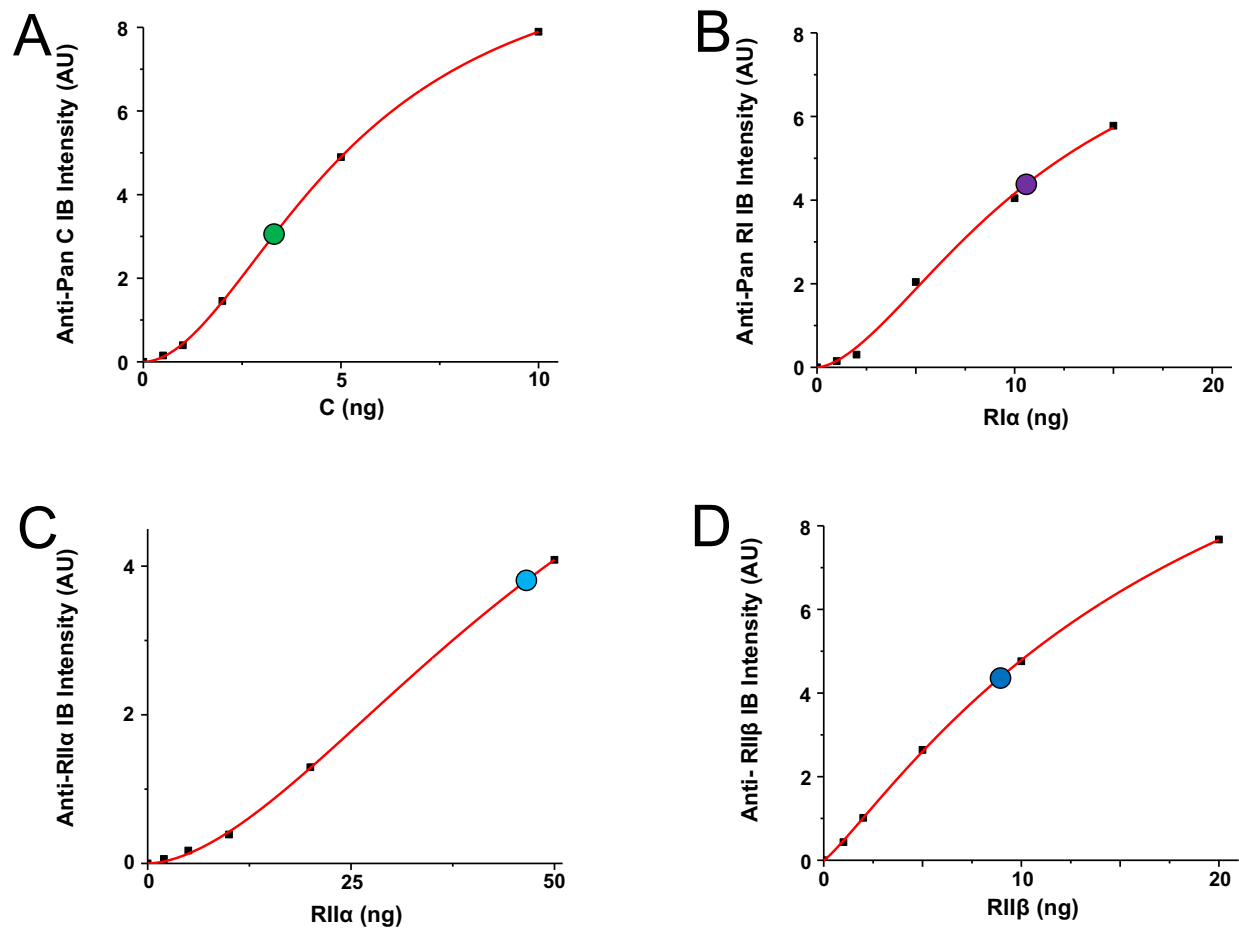
1142

Figure 2-figure supplement 1. Reference curves for quantitation of PKA subunits in CA1 neuropil. The four panels show reference curves (red lines) that relate immunoblot band intensity to ng of PKA subunit per lane, and correspond to the data shown in *Figure 2*C. (**A**) Anti-pan C immunoblot reference curve. The point at which the neuropil extract lane falls on the curve is denoted by a green circle. (**B**) Anti-pan RI reference curve with neuropil extract lane denoted by a purple circle. (**C**) Anti-RIIα reference curve with neuropil extract lane denoted by a light blue circle. (**D**) Anti-RIIβ reference curve with the neuropil extract lane denoted by a dark blue circle.

E Maximal 520/485 nm emission ratio changes (% change min⁻¹)

	cAMP Concentration (nM)					
	0	100	200	500	1000	2000
Type II PKA only	0.46±0.33 (n=3)	1.67±1.11 (n=3)	4.58±3.40 (n=4)	12.92±5.51 (n=4)	20.31±0.63 (n=9)	28.70±0.49 (n=3)
Type II PKA + CN	0.34±0.15 (n=3)	0.78±0.44 (n=3)	3.75±1.93 (n=4)	11.39±4.94 (n=4)	16.26±0.48 (n=19)	27.04±1.88 (n=3)
Type II PKA + CN + AKAP79$_{c97}$	0.00±0.03 (n=3)	0.19±0.10 (n=3)	1.63±0.68 (n=4)	4.28±2.05 (n=4)	7.67±0.32 (n=25)	13.52±1.34 (n=3)

Figure 3-figure supplement 1. AKAR4 reference measurements with PKA catalytic subunit. (**A**) Averaged AKAR4 traces showing change in 520 nm / 485 nm (Y/C) emission ratio over time after injection of 5 mM ATP into reactions containing only PKA C subunits at a range of concentrations. (**B**) Relationship between free C subunit concentration (in the absence of CN) and emission ratio change per minute. The data was fitted to a Hill function (y = 380*x$^{1.71}$/(3481$^{1.71}$+x$^{1.71}$) with an adjusted R-square value of 0.99983. (**C**) Averaged AKAR4 traces showing data for the same experiment as the preceding panel but with 1.5 μM CN included in all reactions. (**D**) Peak 520 nm / 485 nm (Y/C) emission ratio changes at different concentrations of C subunit, either without (black bars) or with (striped bars) 1.5 μM CN. Average rates were calculated between 15-75 s, with the exception of 0 and 25 nM C subunit concentrations (30 – 330 s). (**E**) Averaged peak AKAR4 responses from all recordings for type II PKA either alone (top row), with CN (middle row), or with both CN and AKAP collected after injections of 5 mM ATP with different concentrations of cAMP. These rates were cross-referenced against the reference curve shown in panel b to estimate free C subunit concentrations (plotted in *Figure 4*A-C). Peak rates were calculated between 30-90 s, with the exception of 0 & 100 nM cAMP responses where a wider time window (30-330 s) was applied.
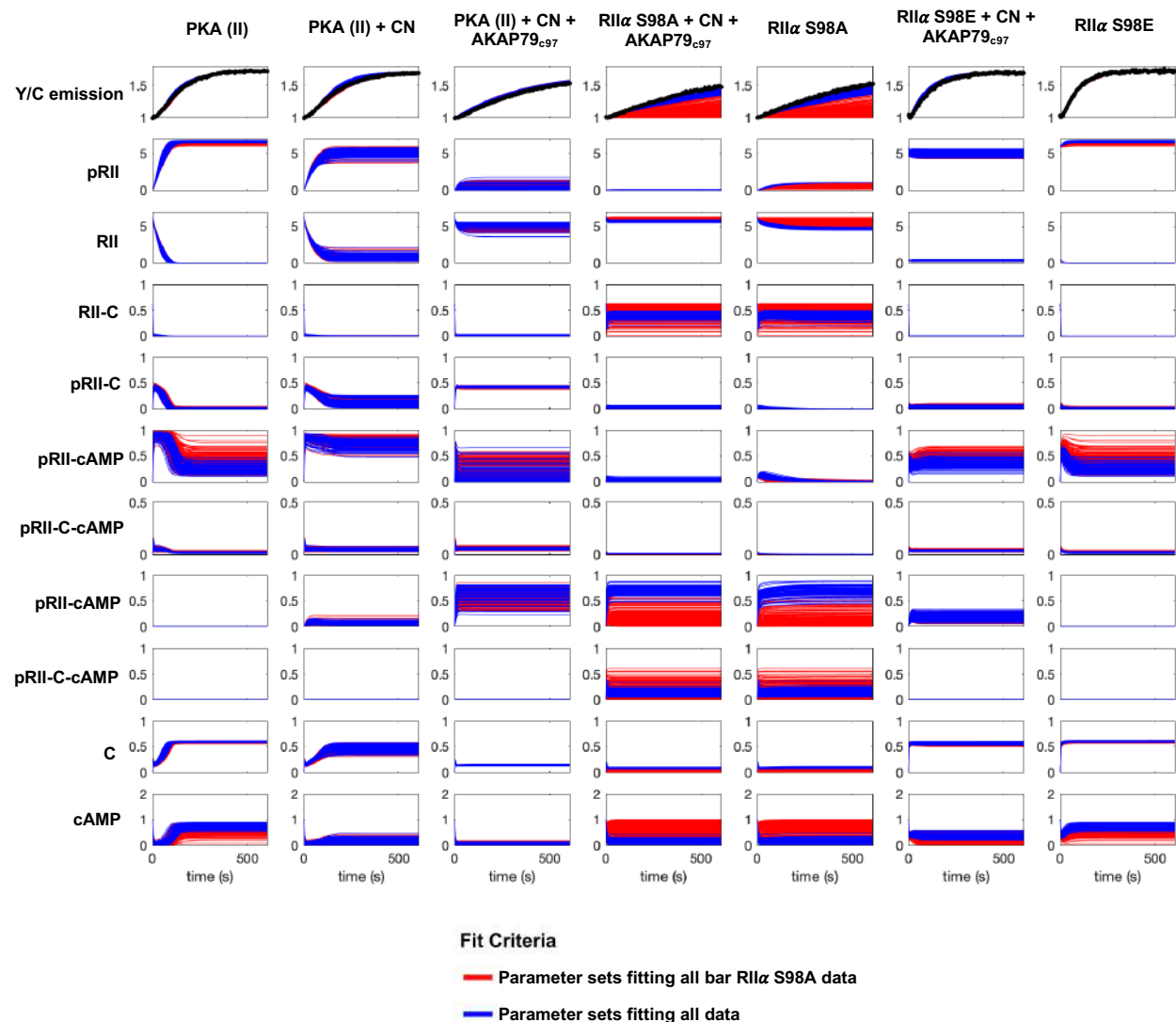
1168

1169

1170

1171 **Figure 4-figure supplement 1. Simulations of kinetic scheme species changes in concentration over time.**
1172 Each row corresponds to the concentration (μM) of an individual species simulated in seven different reaction
1173 mixtures. The first three columns correspond to experiments with WT RIIα subunits; columns four and five to
1174 experiments with RIIα S98A subunits, and the last two columns with RIIα S98E subunits. Red lines correspond
1175 to simulations whose parameter sets were classified as far from experimental data collected with mutated RIIα,
1176 but which fit well to data collected with WT RIIα subunits in reactions stimulated with 1 or 2 μM cAMP. Blue
1177 traces correspond to simulations with parameter sets that generated results close to experimental data collected
1178 with both WT and mutant RIIα subunits.

1179
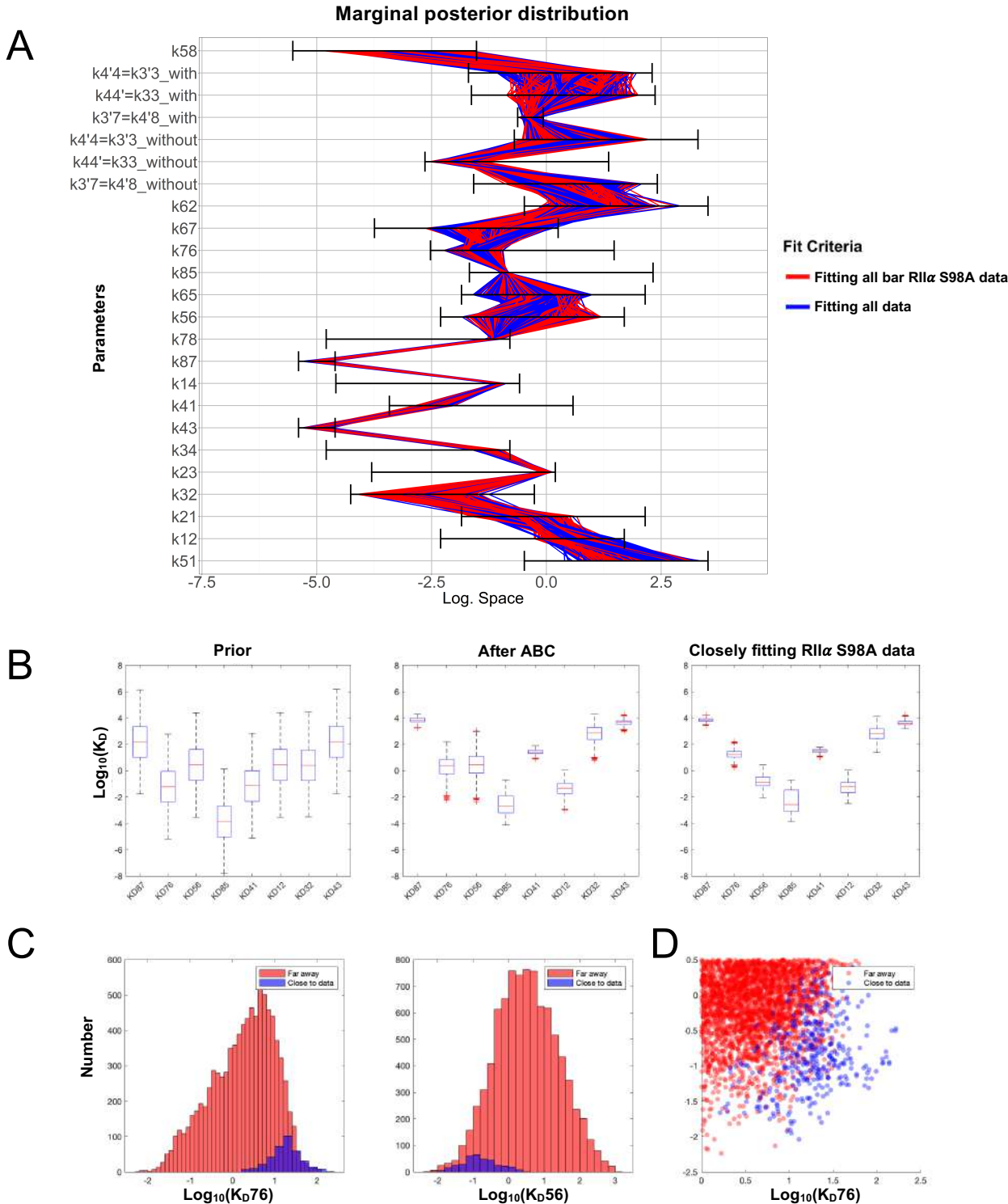
Figure 5-figure supplement 1. Space of parameters used in model fitting. (**A**) The illustration shows the marginal posterior distribution of each model parameter on a logarithmic scale for a subset of parameter samples that generated simulations that fit experimental data collected with WT RIIα subunits. Each sample in the distribution is connected across the parameters by a line, whose color indicates whether the corresponding

1186   parameter set also generated simulations fitting closely (blue) to data collected with mutant RIIα subunits or

1187   not (red). The parameter priors are indicated by the respective black horizontal bars. It can be noted that the

1188   following CN-related parameters are always equal: *k4'4 = k3'3, k44'=k33',* and *k3'7=k4'8* for each sample.

1189   (**B**) Distribution of dissociation constants (K_D's). The boxplots display median values (red lines), the 50 %

1190   datapoint distribution around the median (designated by boxes) and the remaining 25% datapoint distributions

1191   (lower and upper whiskers). Boxplots are shown for all eight K_D's obtained with the model priors (left), data

1192   fitted using experiments with WT RIIα subunits (middle), and parameters selected for fitting to data collected

1193   with RIIα S98A subunits. (**C**) Marginal histograms for K_D76 (left) and K_D56 (right) with parameter sets

1194   classified according to whether they fit well to the RIIα S98A data (blue) or not (red). (**D**) Scatterplot showing

1195   how the K_D76 and K_D56 parameters are related according to the same two classes.

1196

1197

1198

1199

1200 **Supplementary Table 1. Kinetic modeling parameters**. The table lists parameters used in computational
1201 modeling. Parameters terminology is according to the numbers above states in *Figure 4*B, e.g., k12 refers to
1202 the on rate of cAMP binding to state *1* (pRII-C) to produce state *2* (pRII-C-cAMP). The prior range used to
1203 initially constrain parameter estimation is provided for each parameter along with links to the references used
1204 to define these ranges.
1205

Parameter	Value	Parameter Range for ABC	Reference
Parameters for phosphorylated RII subunits			
k12 (pRII-C + cAMP → pRII-C-cAMP)	0.496 $\mu M^{-1} s^{-1}$	4.96e-03 to 4.96e+01 $\mu M^{-1} s^{-1}$	(Isensee et al., 2018)
k21 (pRII-C + cAMP ← pRII-C-cAMP)	1.43 s^{-1}	1.43e-02 to 1.43e+02 s^{-1}	
k23 (pRII-cAMP + C → pRII-C-cAMP)	1.56e-02 $\mu M^{-1} s^{-1}$	1.56e-04 to 1.56 $\mu M^{-1} s^{-1}$	(Zhang et al., 2012)
k32 (pRII-cAMP + C ← pRII-C-cAMP)	5.40e-03 s^{-1}	5.45e-05 to 5.45e-01 s^{-1}	
k43 (pRII + cAMP → pRII-cAMP)	1.0e-05 $\mu M^{-1} s^{-1}$	4.0e-06 to 2.50e-05 $\mu M^{-1} s^{-1}$	(Ogreid & Doskeland, 1981)
k34 (pRII + cAMP ← pRII-cAMP)	1.60e-03 s^{-1}	1.60e-05 to 1.60e-01 s^{-1}	
k41 (pRII + C → pRII-C)	3.8e-02 $\mu M^{-1} s^{-1}$	3.80e-04 to 3.8 $\mu M^{-1} s^{-1}$	(Zhang et al., 2015)
k14 (pRII + C ← pRII-C)	2.60e-03 s^{-1}	2.60e-05 to 2.60e-01 s^{-1}	
Parameters for dephosphorylated RII subunits			
k56 (RII-C + cAMP → RII-C-cAMP)	0.496 $\mu M^{-1} s^{-1}$	4.96e-03 to 49.6 $\mu M^{-1} s^{-1}$	(Isensee et al., 2018)
k65 (RII-C + cAMP ← RII-C-cAMP)	1.43 s^{-1}	1.43e-02 to 1.43e+02 s^{-1}	
k76 (RII-cAMP + C → RII-C-cAMP)	2.98e-01 $\mu M^{-1} s^{-1}$	2.98e-03 to 2.984e+01 $\mu M^{-1} s^{-1}$	(Zhang et al., 2015; Zhang et al., 2012)
k67 (RII-cAMP + C ← RII-C-cAMP)	1.80e-02 s^{-1}	1.80e-04 to 1.80 s^{-1}	
k87 (RII + cAMP → RII-cAMP)	1.0e-05 $\mu M^{-1} s^{-1}$	4.0e-06 to 2.5e-05 $\mu M^{-1} s^{-1}$	(Ogreid & Doskeland, 1981)
k78 (RII + cAMP ← RII-cAMP)	1.60e-03 s^{-1}	1.60e-05 to 1.60e-01 s^{-1}	
k85 (RII + C → RII-C)	2.10 $\mu M^{-1} s^{-1}$	2.10e-02 to 2.1e+02 $\mu M^{-1} s^{-1}$	(Zhang et al., 2015)
k58 (RII + C ← RII-C)	3.0e-04 s^{-1}	3.0e-06 to 3.0e-02 s^{-1}	
Parameters for phosphorylation of RII subunits			
k51 (RII-C → pRII-C)	33 s^{-1}	3.30e-01 to 3.30e+03 s^{-1}	(Moore et al., 2003)
k62 (RII-C-cAMP → pRII-C-cAMP)	33 s^{-1}	3.30e-01 to 3.30e+03 s^{-1}	
Parameters for dephosphorylation of RII subunits			
k44' (pRII + CaN → pRII-CaN)	0.226 $\mu M^{-1} s^{-1}$	2.26e-03 to 2.26e+01 $\mu M^{-1} s^{-1}$	(Stemmer & Klee, 1994)
k4'4 (pRII + CaN ← pRII-CaN)	20 s^{-1}	2.0e-01 to 2.0e+03 s^{-1}	
k33' (pRII-cAMP + CaN → pRII-cAMP-CaN)	0.226 $\mu M^{-1} s^{-1}$	2.26e-03 to 2.26e+01 $\mu M^{-1} s^{-1}$	Equal to k44'
k3'3 (pRII-cAMP + CaN ← pRII-cAMP-CaN)	20 s^{-1}	2.0e-01 to 2.0e+03 s^{-1}	Equal to k4'4

k4'8 (pRII-CaN $\rightarrow$ RII + CaN)	2.6 s^{-1}	2.6e-02 to 2.6e+02 s^{-1}	(Stemmer
k3'7 (pRII-cAMP-CaN $\rightarrow$ RII-cAMP + CaN)	2.6 s^{-1}	2.6e-02 to 2.6e+02 s^{-1}	& Klee, 1994)
Parameters for dephosphorylation of RII subunits when AKAP79 is present			
k44'-AKAP (pRII + CaN $\rightarrow$ pRII-CaN)	2.33 μM^{-1} s^{-1}	2.33e-02 to 2.33e+02 μM^{-1} s^{-1}	This study
k4'4-AKAP (pRII + CaN $\leftarrow$ pRII-CaN)	2 s^{-1}	2.0e-02 to 2.0e+02 s^{-1}	
k33'-AKAP (pRII-cAMP + CaN $\rightarrow$ pRII-cAMP-CaN)	2.33 μM^{-1} s^{-1}	2.33e-02 to 2.33e+02 μM^{-1} s^{-1}	Equal to k44'-AKAP
k3'3-AKAP (pRII-cAMP + CaN $\leftarrow$ pRII-cAMP-CaN)	2 s^{-1}	2.0e-02 to 2.0e+02 s^{-1}	Equal to k33'-AKAP
k4'8-AKAP (pRII-CaN $\rightarrow$ RII + CaN)	0.45 s-1	0.237 to 0.855 s^{-1}	This study
k3'7-AKAP (pRII-CaN $\rightarrow$ RII + CaN)	0.45 s-1	0.237 to 0.855 s^{-1}	This study
Parameters for AKAR4 phosphorylation			
AKAR4 + C $\rightarrow$ AKAR4-C	1.82e-02 μM^{-1} s^{-1}	Fixed	This study
AKAR4 + C $\leftarrow$ AKAR4-C	0.106 s^{-1}	Fixed	
AKAR4-C $\rightarrow$ pAKAR4 + C	10.2 s^{-1}	Fixed	

1206
1207
1208

1209 **Supplementary Table 2. Oligonucleotide primer sequences**
1210

Primer Name	Sequence (5' to 3')
EcoI_8HisNLS_XbaI	AATTCGCCGGCCACCACCACCACCACCACCACCACGGCGCCCTGCCCCCCCCTGGAGCGCCTGACCCTGTAAT
XbaI_8HisNLS_EcoRI	CTAGATTACAGGGTCAGGCGCTCCAGGGGGGGCAGGGCGCCGTGGTGGTGGTGGTGGTGGTGGCCGGCG
XbaI_8HisNLS_EcoRI	CTAGATTACAGGGTCAGGCGCTCCAGGGGGGGCAGGGCGCCGTGGTGGTGGTGGTGGTGGTGGCCGGCG
Nde1_AKAP79_331	CATGGCAGCCATATGCATCATCACCATCATCATAAAAGAATGGAGCCAATTG
Nde1_AKAP79_1	CATGGCAGCCATATGCATCATCACCATCATCATATGAGCCACATCCAGATCC
AKAP79_427_EcoRI	ACAGAATTCTCACTGTAGAAGATTGTTTATTTTATTATCATCAGAG
hS98A_F	GATTTAATAGACGAGTAGCAGTCTGTGCTGAGACC
hS98A_R	GGTCTCAGCACAGACTGCTACTCGTCTATTAAATC
hS98E_F	CTAGCAGATTTAATAGACGAGTAGAAGTCTGTGCTGAGACCTATAACCCTG
hS98E_R	CAGGGTTATAGGTCTCAGCACAGACTTCTACTCGTCTATTAAATCTGCTAG
ΔPKA_F	GAGGATAGAACTTCAGAACAATATGAAACAAAGAATGCTATTCAGTTGTCAATAGAAC
ΔPKA_R	GTTCTATTGACAACTGAATAGCATTCTTTGTTTCATATTGTTCTGAAGTTCTATCCTC
Prkar2a_F	TAGAATTCCACATGAGCCACATCCAGATCCCAC
Prkar2a_R	TAGGATCCGAGCTACTGCCCGGGGTCCAATAGATC
Prkar2a_shRNA_resist_F	GCGAGGCCCGCCGGCAAGAGTCAGACTCGTTCA
Prkar2a_shRNA_resist_R	TGAACGAGTCTGACTCTTGCCGGCGGGCCTCGC
shRIIα_F1	GCCAGGAATCAGACTCGTTCATTCAAGAGATGAACGAGTCTGATTCCTGGCTTTTTTGT
shRIIα_R1	CTAGACAAAAAAGCCAGGAATCAGACTCGTTCATCTCTTGAATGAACGAGTCTGATTCCTGGC
shRIIα_2F	GGAAGCCTGTAAAGACATTTTCAAGAGAAATGTCTTTACAGGCTTCCTTTTTTGT
shRIIα_2R	CTAGACAAAAAAGGAAGCCTGTAAAGACATTTCTCTTGAAAATGTCTTTACAGGCTTCC
shRIIα_3F	GGCAGTAGATGTGATGAATTTCAAGAGAATTCATCACATCTACTGCCTTTTTTGT
shRIIα_3R	CTAGACAAAAAAGGCAGTAGATGTGATGAATTCTCTTGAAATTCATCACATCTACTGCC
shScram_F	GCCACGTCATAGAGACACTGTTTCAAGAGAACAGTGTCTCTATGACGTGGCTTTTTTGT
shScram_R	CTAGACAAAAAAGCCACGTCATAGAGACACTGTTCTCTTGAAACAGTGTCTCTATGACGTGGC
rS97A_F	CCAGCAAATTTACTAGACGAGTAGCAGTCTGTGCAGAAAC
rS97A_R	GTTTCTGCACAGACTGCTACTCGTCTAGTAAATTTGCTGG
rS97E_F	CCGATTCCCAGCAAATTTACTAGACGAGTAGATGTCTGTGCAGAAACGTT
rS97E_R	AACGTTTCTGCACAGACATCTACTCGTCTAGTAAATTTGCTGGGAATCGG
RIIα-IRES-EGFP_F	GACGAGCTGTACAAGTAAACCGGTGCGGCCGCGACTCTAGATCATAATCAGCCATACCACATTTGTAGA
RIIα-IRES-EGFP_R	TCTACAAATGTGGTATGGCTGATTATGATCTAGAGTCGCGGCCGCTGGCCATTTACTTGTACAGCTCGTC
FUGW_NheI_F	GGCTGCTGGGCTAGCCGGGGCTTTC
FUGW_NheI_R	GAAAGCCCCGGCTAGCCCAGCAGCC

1211

1212